4

Plastic Resistance of Thin-walled Prismatic Tubes under Large Twisting Rotations

by

Weigang Chen

Submitted to the Department of Ocean Engineering and
the Department of Mechanical Engineering
in Partial Fulfillment of the Requirement for the Degrees of
Master of Science in Mechanical Engineering
and
Master of Science in Ocean Engieering
at the
MASSACHUSETTS INSTITUTE OF TECHNOLOGY
June 2000

Author.....
Weigang Chen
May 1, 2000

Certified by.....
Tomasz Wierzbicki
Professor of Applied Mechanics
Thesis Supervisor

Read by.....
Frank McClintock
Professor of Mechanical Engineering
Thesis Reader

Accepted by.....
kalakis
Chairman mittee

Accepted by.....
. Sonin
Chairperson, Department Committee on Graduate Studies
Department of Mechanical Engineering

Contents

List of Figures

List of Tables

Plastic Resistance of Thin-walled Prismatic Tubes under Large Twisting Rotations

Weigang Chen

Submitted to the Department of Mechanical Engineering and
the Department of Ocean Engineering in April 2000, in partial fulfillment of the
requirements for the degrees of
Master of Science in Mechanical Engineering
and
Master of Science in Ocean Engineering

Abstract

Torsional collapase of thin-walled prismatic tubes is studied analytically and numerically. Simple torsional buckling models are developed to predict the plastic resistance of square tubes under large plastic rotation using energy method. By considering the combined effect of geometry and material, the onset of the sectional plastic buckling is predicted and the critical twisting rotation for sectional buckling is obtained. Next, an analytical expression is derived for the moment-rotation relation valid for normalized rotation up to 0.393. The analytical solution is shown to compare well with the numerical results. The solutions are then extended for rectangular and hexagonal thin-walled tubes. Numerical simulations for rectangular and hexagonal tubes are also carried out and the results are presented in this paper for the purpose of comparison. Finally, torsional experiments are conducted on aluminum extrusion members and results are compared with analytical and numerical solutions with reasonable agreement.

Thesis Supervisor: Tomasz Wierzbicki
Titile: Professor of Applied Mechanics
Thesis Reader: Frank McClintock
Title: Professor of Mechanical Engineering

Nomenclature

b	column width
t	wall thickness
l	column length
E	Young's modulus
σ_y	initial yield stress
ν	Poisson's ratio
σ_0	plastic flow strength
V_c	dilatational wave speed
K	bulk modulus
θ_0	end twisting rotation
$\bar{\theta_0}$	nomalized twisting rotation, $\bar{\theta_0} = \frac{b\theta_0}{2l}$
$\dot{\theta_0}$	rate of end twisting rotation
T	physical twisting moment
τ	dimensionless twisting moment, $\tau = \frac{T}{2\sigma_0 b^2 t}$
δt	time step in numerical simulation
L^e	characteristic length of element
ρ	mass density
$N_{\alpha\beta}$	membrane stress tensor
$\epsilon_{\alpha\beta}$	strain tensor
$\dot{\epsilon_{\alpha\beta}}$	strain rate tensor
$\sigma_{\alpha\beta}$	stress tensor
C	material constant in stress-strain relation
n	exponent in stress-strain relation
$\dot{\kappa}$	plastic flow constant
v	displacement in y-direction
w	displacement in z-direction
U_0	axial displacement of column
r	width-length ratio of tube, $r = b/l$
R	equivalent width-length ratio in deformation-spreading
A	geometrical parameter in the buckling model
δ	geometrical parameter in the buckling model
θ_c	critical twisting rotation (radian)
θ_m	transitional twisting rotation
ξ	half length of the most-deformed area

Chapter 1

Introduction

The problem of a large plastic collapse of cross-sections of thin-walled prismatic tubes subjected to different loading conditions has received a great deal of attention over the past twenty years. Theoretical predictions are available for bending and axial crushing cases. For example, Wierzbicki and Abramowicz [1] developed a theory for plastic resistance of a rectangular box tube undergoing a pure axial crushing load. For bending deformation, theoretical solutions were derived by Kecman [2], Abramowicz [3], and more recently by Wierzbicki [4].

The torsional behavior of thin-walled beams or tubes well beyond the maximum torque is of interest in many applications. For example, in a side impact of a car, the bending collapse of the B-pillar may induce twisting deformation on the roof rail (see Fig.1.1, the space frame structure of Audi A8).

The maximum load under torsion or combined loading has been studied over the past years. Baba [5] developed a finite element formulation for stress analysis of a twisting bar with a solid or a thin-walled section. The formulation can be applied to elastic-plastic pure-torsion or warping-torsion problems with small displacement. Murray [6] studied a single rectangular plate subjected to pure torsion, bending and compressive loading. The uncoupled solutions were later extended to combined loading in the case of compressive and torsional moment [7], and torsion and bending moment [8]. Grant [9] proposed a solution to the thin-walled sections undergoing

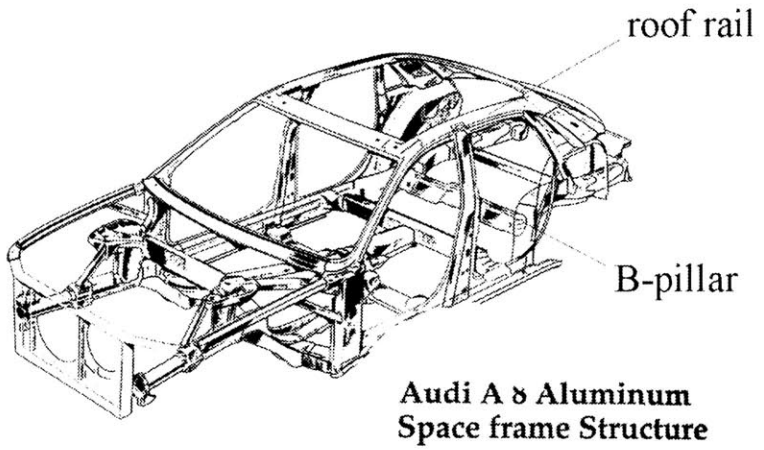

Figure 1.1: An illustration of Audi A8 space frame structure

uniform torsion. This reference information was reported by Santosa [10], but the author can not locate the article. Ma [11] carried out an experimental study of the static and dynamic plastic buckling of circular cylindrical shells under impact torque using the Hopkinson torsional bar. The static and dynamic critical torque of the shells were determined experimentally. All the aforementioned theorectical analyses developed for the torsion problems were restricted to prectict the onset of local buckling. Trahair [12] developed a method to analyze the plastic torsion behavior of monosymmetric I-sections, lipped and unlipped channels, and equal flange lipped angles, and of point-symmetric lipped and unlipped Z-sections. Recently, Santosa and Wierzbicki [10] conducted numerical simulations for empty boxes and the tubes with light metal filler using a nonlinear finite element code. Three parameters, which are initial crushing moment, the stabilized torsional crushing moment and the critical twisting rotation, were defined to characterize the torsional behavior of empty box tubes.

In this thesis, a theoretical solution is proposed for the torsional behavior of thin-walled square tubes in the range of large normalized rotation up to 0.393. Simple torsional cross-sectional buckling models are developed, which capture the basic torsional crushing mechanisms of thin-walled tubes. The pre-buckling, plastic buckling and post-buckling behavior of square tubes are predicted using least upper bound method. Approximate formulas for the torsional resistance are derived and the solutions are compared with the numerical results. The analytical solution for the square

tubes is then extended to rectangular and hexagonal thin-walled tubes. Numerical simulations for rectangular and hexagonal tubes were also carried out and the results are presented for comparison with the analytical solutions. Finally, experiments were conducted to test the analytical and numerical solutions.

It should be noted that the present research has been reported by the author and his supervisor in references [13, 14, 15, 16].

Chapter 2

Numerical Solutions of Thin-walled Square Tubes

The torsional crushing problem of thin-walled square tubes will be solved numerically in this chapter by using the non-linear explicit finite element code PAM-CRASH. The finite element modelling and simulation techniques are reviewed first. The twisting deformation pattern of the tube and the sectional buckling mode are then illustrated. Finally, the torsional plastic resistance of tubes with various length-width ratios are revealed at large twisting rotations up to 180^0. Santosa and Wierzbicki [10] conducted numerical simulations for empty thin-walled box tubes undergoing torsion using non-linear explicit finite element code PAM-CRASH. The numerical study is continued in present research.

2.1 Finite Element Modelling

The considered tube has length l, width b and wall thickness t, with $l/b = 4 \backsim 6.5$ and $b/t = 50$. The end twisting rotation is denoted by θ_0 (see Fig.2.1). The tube wall was modeled with Belytschko-Tsay-4-node thin shell elements with reduced integration points (see Fig.2.2). Clamped boundary condition was applied at one end of the tube, while the other end was connected to a rigid body mechanism. The rigid body

was allowed to rotate about the x-axis and move in x direction. By connecting to this rigid-body mechanism, warping at the end section was prevented. The velocity of twisting rotation was applied at the center of gravity of the rigid body.

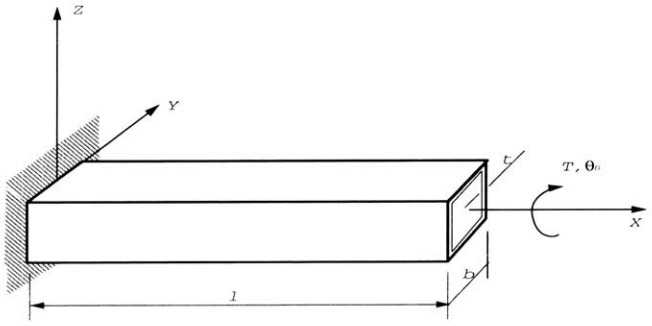

Figure 2.1: A thin-walled square tube under torsional loading

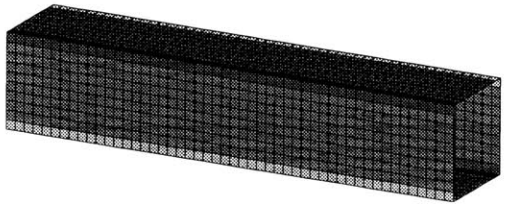

Figure 2.2: Finite Element Model of the tube

Self impact contact (type 36 in PAM-CRASH) was utilized to simulate the contact between walls of the tube during large twisting deformation.

The constitutive behavior of the thin shell element for the tube material was based on the elastic-plastic material model with Von-Mises' isotropic plasticity algorithm. The transverse shear effect was also considered by this material model. Plastic hardening was described by a multi-linear curve, in which pairs of the plastic tangent modulus and the plastic stress were specified.

Table 2.1: Strain hardening data for AA6063 T7

Plastic Strain	Plastic Stress [MPa]	Plastic Modulus [MPa]
0.00000	86.94	33390.0
0.00027	95.94	2913.0
0.00211	101.30	2200.0
0.00575	109.30	1959.0
0.01493	127.30	1460.0
0.02630	149.30	594.1
0.06939	169.50	18.0
0.15270	171.00	0.0

The material used in the calculation was the aluminum extrusion AA6063 T7, which is commonly used for automotive structures, with mechanical properties of Young's modulus $E = 69GPa$, initial yield strength $\sigma_y = 86.94MPa$, Poisson's ratio $\nu = 0.3$. The strain hardening data are given in Table2.1. The engineering stress-strain data were converted to true stress-strain data for finite element calculation.

2.2 Quasi-static Simulation

There are two time integration algorithms in dynamic finite element analysis, namely, explicit and implict. In the explicit approach, internal and external forces are summed at each node, and a nodal acceleration is computed by dividing by nodal mass. The solution is advanced by integrating this acceleration in the time domain. The maxiumum time step size is limited by the Courant conditon, which requires that solution spreading speed can not exceed the dilatational wave speed V_c in the material [17, 18].

$$V_c = \sqrt{\frac{3K(1-\nu)}{\rho(1+\nu)}} \tag{2.1}$$

where K is the bulk modulus; ρ denotes mass density and ν is Poisson's ratio.

Therefore, the explicit algorithm typically requires many relatively inexpensive time steps. In constrast, implicit simulation typically involves a relatively small number of expensive time steps due to iterative process at each time step. The maximum stable size of time step in an explicit dynamic analysis is imposed by above Courant condition

$$\Delta t = \frac{L^e}{V_c} = L^e \sqrt{\frac{\rho(1+\nu)}{3K(1+\nu)}} \tag{2.2}$$

where L^e is the characteristic length of element.

While explict analysis is well suited to dynamic simulation such as impact and crash, it can become prohibitively expensive to conduct long duration analysis. In order to use explicit code such as PAM-CRASH for quasi-static analysis, a special numerical technique has to be applied to simulate the process in a shortest time period while inertia effect remains insignificant. In the current study, the mass scaling method was utilized. In this approach, mass density of the material was scaled down by a factor of n^2 so that the inertial forces will be negligible. However, scaling down the mass density results in a smaller time step, according to Eq.(2.2), by a factor of n. The analysis will hence take many more time steps. To limit the number of time steps, the loading rate has be be increased. In the current analysis, the material density was decreased by 1000 times, while the loading rate was applied at an angular velocity of $\omega = 100\pi \ rad/s$.

Care has to be taken to ensure that the kinetic energy should be far smaller than the internal energy over the period of simulation so that the process can be considered as a quasi-static one. Moreover, hour-glass instability may appear in finite elements with reduced integration points (some deformation modes result in zero nodal forces when the nodal forces are computed by a single point integration). Therefore, a sufficiently fine mesh has be to used to avoid an hour-glass instability. Hour-glass energy needs to be checked to ensure it is negligible compared to the internal energy of the system.

Although via the mass scaling method, the quasi-static problems can be solved efficiently by explicit finite element code, caution must be taken in applying this method. Both the kinetic energy and hour-glass energy must be well-controlled (one or two

order of magnitude smaller than internal energy) to ensure the accuracy of the numerical solutions.

2.3 Deformation Pattern

Square tubes with wall thickness $t = 1mm$, width-thickness ratio $b/t = 50$, and length-width ratio $l/b = 4 \backsim 6.5$ were considered in the numerical calculation. The deformed shape of the tube with $l/b = 5$ at 45^o rotation is illustrated in Fig.2.3. The evolution of the shape at the mostly deformed cross-section is shown in Fig.2.4. The following conclusions can be drawn from the analysis of the above figures.

(i) In the pre-buckling stage, all sections rotate without sectional buckling. The resistance is derived from shear stresses that increase because of first elasticity and then strain-hardening with the increasing rotation angle.

(ii) After buckling, the walls deform inwards with an increasing amplitude w_0 of the transverse displacement function $w(x_\alpha)$. This reduces shear stresses and changes the geometry so that the torsional resistance drops by a factor of 2 to 3 relative to the pre-buckling state.

(iii) At a certain deflection amplitude and rotation angle, internal touching occurs which locally stiffens a given cross-section. From this point on, torsional deformation spreads along the length of the tube causing a moderate increase of the torque.

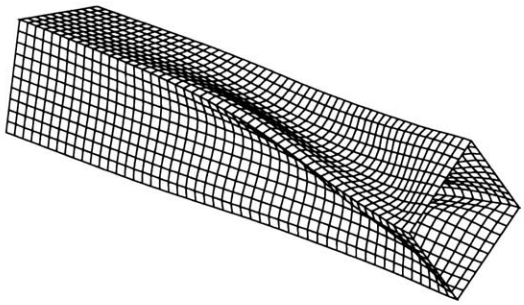

Figure 2.3: Deformed shape of the thin-walled square tube at 45^o rotation (normalized rotation 0.0785)

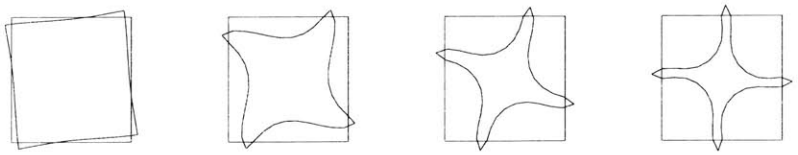

Figure 2.4: Evolution of the shape at the mostly deformed cross-section

2.4 Plastic Resistance

The torsional plastic resistances of tubes with $t = 1mm$, $b/t = 50$ and $l/b = 4 \backsim 6.5$ are plotted in Fig.2.5 at rotation angles up to 180^o. It can be seen that the twisting moment reached an ultimate value approximately at a twisting rotation of 10^o. Subsequently, the torsional resistance dropped significantly with increasing twisting rotation due to the plastic sectional buckling of the tube. At large rotations, the twisting moment appeared to reach a constant asymptotic value.

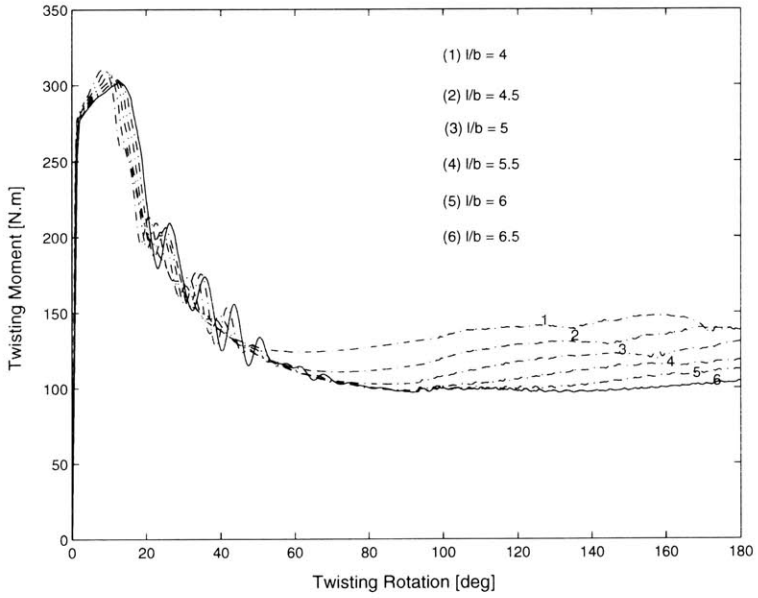

Figure 2.5: Torsional plastic resistance of thin-walled square tubes (To normalize, plot $\frac{T}{2\sigma_0 b^2 t}$ vs $\frac{b\theta_0}{l}$ with $\sigma_0 = 105.4MPa$, $t = 1mm$ and corresponding b and l)

Chapter 3

An Approximate Solution for Thin-walled Square Tubes in Torsion

The torsional crushing of thin-walled square tubes will be modelled analytically in this chapter. A kinematic approach is utilized in the analysis based on the principle of virtual work. Pre-buckling, cross-section deforming and deformation-spreading mechanisms are proposed as three phases of torsional deformation. A kinematically admissible displacement field is established in each phase of deformation and a closed-form solution for torque is obtained. By considering the combined effect of the geometry and material, the critical twisting rotation to plastic buckling is determined analytically. Because the kinematic approach is applied in the current analysis, the obtained plastic resistance establishes the upper bound of the limit load carrying capacity of the tubes.

3.1 Theoretical Formulation

A kinematic approach is proposed in the present study based on assumed displacement fields and the principle of virtual work

$$T \cdot \dot{\theta}_0 = \int_S N_{\alpha\beta} \cdot \dot{\epsilon}_{\alpha\beta} dS \tag{3.1}$$

where T is the twisting moment applied at the end of the tube; $N_{\alpha\beta}$ and $\dot{\epsilon}_{\alpha\beta}$ are respectively components of the membrane stress tensor and strain rate tensor in the tube wall. Two material models are introduced. For the analysis of the plastic buckling load, the material is assumed to be rigid-plastic, strain-hardening obeying a power law $\bar{\sigma} = C\bar{\epsilon}^n$ and the Von Mises yielding condition, where $\bar{\sigma}$ and $\bar{\epsilon}$ are respectively the equivalent stress and strain. The post-buckling analysis is based on the rigid-perfectly plastic model. The components of the strain rate tensor in the local in-plane coordinate system $\alpha, \beta = 1, 2$ are

$$\dot{\epsilon}_{\alpha\beta} = \begin{pmatrix} \dot{\epsilon}_{xx} & \dot{\epsilon}_{xy} \\ \dot{\epsilon}_{yx} & \dot{\epsilon}_{yy} \end{pmatrix} \tag{3.2}$$

where x is aligned with the longitudinal axis of the tube. Components $\dot{\epsilon}_{xx}$ and $\dot{\epsilon}_{xy}$ can be evaluated from the assumed deformation modes and are related to the twisting rotation $(\theta_0, \dot{\theta}_0)$. The tensor of membrane stress $N_{\alpha\beta}$ is determined from the associated flow rule. To take strain hardening effect into account in the rigid-perfectly plastic model, the work equivalent flow strength is used in the calculation, [19], [20]

$$\sigma_0 = \sqrt{\frac{\sigma_y \sigma_u}{n+1}} \tag{3.3}$$

where σ_y and σ_u are the yield and ultimate strength of the material, respectively; n denotes the power law exponent of the material.

The Von Mises yielding condition in a plane stress field is

$$F \equiv \sigma_{xx}^2 + \sigma_{yy}^2 - \sigma_{xx}\sigma_{yy} + 3\tau_{xy}^2 - \sigma_0^2 = 0 \tag{3.4}$$

The strain rate can be calculated from the associated flow rule

$$\dot{\epsilon}_{\alpha\beta} = \dot{\kappa}\frac{\partial F}{\partial \sigma_{\alpha\beta}} \tag{3.5}$$

where $\dot{\kappa}$ is flow constant at one point (Eq.(3.7)) over different coordinates, but varies in space and time.

The components of stress tensor $\sigma_{\alpha\beta}$ can be expressed in terms of the proportionality constant $\dot{\kappa}$ and the strain rate tensor $\dot{\epsilon}_{\alpha\beta}$ by inverting Eq.(3.5)

$$\begin{aligned} \sigma_{xx} &= \frac{1}{3\dot{\kappa}}(\dot{\epsilon}_{yy} + 2\dot{\epsilon}_{xx}) \\ \sigma_{yy} &= \frac{1}{3\dot{\kappa}}(\dot{\epsilon}_{xx} + 2\dot{\epsilon}_{yy}) \\ \tau_{xy} &= \frac{1}{3\dot{\kappa}}\dot{\epsilon}_{xy} \end{aligned} \tag{3.6}$$

The constant $\dot{\kappa}$ can now be determined by substituting Eq.(3.7) into Eq.(3.4)

$$\dot{\kappa} = \frac{1}{\sqrt{3}\sigma_0}\sqrt{\dot{\epsilon}_{xx}^2 + \dot{\epsilon}_{yy}^2 + \dot{\epsilon}_{xx}\dot{\epsilon}_{yy} + \dot{\epsilon}_{xy}^2} \tag{3.7}$$

The rate of plastic work per unit volumn is $\sigma_{\alpha\beta}\dot{\epsilon}_{\alpha\beta}$, which can be expanded into the following form

$$\sigma_{\alpha\beta}\dot{\epsilon}_{\alpha\beta} = \sigma_{xx}\dot{\epsilon}_{xx} + \sigma_{yy}\dot{\epsilon}_{yy} + 2\tau_{xy}\dot{\epsilon}_{xy} \tag{3.8}$$

Substituting Eq.(3.6) and Eq.(3.7) into Eq.(3.8) leads to

$$\sigma_{\alpha\beta}\dot{\epsilon}_{\alpha\beta} = \frac{2\sigma_0}{\sqrt{3}}\sqrt{\dot{\epsilon}_{xx}^2 + \dot{\epsilon}_{yy}^2 + \dot{\epsilon}_{xx}\dot{\epsilon}_{yy} + \dot{\epsilon}_{xy}^2} \tag{3.9}$$

Therefore, Eq.(3.1) can be re-written as

$$T \cdot \dot{\theta}_0 = \frac{2\sigma_0 t}{\sqrt{3}} \int_S \sqrt{\dot{\epsilon}_{xx}^2 + \dot{\epsilon}_{yy}^2 + \dot{\epsilon}_{xx}\dot{\epsilon}_{yy} + \dot{\epsilon}_{xy}^2} dS \tag{3.10}$$

where the integration is taken over the surfaces of the tube. It should be noted that bending and warping resistances are neglected in the current analysis.

3.2 The Deformation Modes

As observed in numerical simulations, sectional buckling occurs when the end rotation reaches a certain angle (critical twisting rotation) and an inward sectional deformation mode is developed in the tube (see Fig.2.4), which reduces stresses and changes the geometry so that the torsional resistance considerably drops. The amplitude of the sectional buckling deformation increases with the increase of twist. At a certain rotation angle, internal touching occurs at the most deformed cross-section which locally stiffens the section. As a result, a most-deformed section is formed. From that point on, this deformation will spread along the length of the tube and thus form a most-deformed area. With these physical understandings, a three-phase deformation mechanism is proposed in the current approximate analysis. The three phases are namely, pre-buckling, cross-section deforming and deformation-spreading. They will be described in the following.

In each phase, a velocity field is assumed and the principle of virtual work (Eq.(3.10)) is applied to evaluate the torsional resistance of the tube. The shell of the tube is assumed to be inextensible in the hoop direction. Thus, $\dot{\epsilon}_{yy} = 0$.

3.2.1 Pre-buckling

In this phase, all sections rotate as rigid bodies without sectional deformation. It is assumed that the rotation angles at sections from the fixed end to the free end are

varying linearly from 0 to the end rotation angle θ_0. Therefore, the walls of the tube become spiral surfaces, as illustrated in Fig. 3.1.

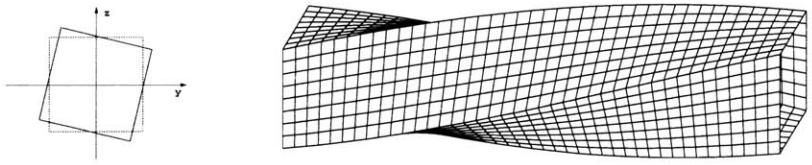

Figure 3.1: Pre-buckling deformation of a square tube under torsion

Consider the upper flange of the tube, the displacement at a cross-section with longitudinal coordinate x can be found from the assumption of the spiral-shape deformation

$$\begin{aligned} u &= 0 \\ v &= y\cos(\frac{\theta_0}{l}x) + \frac{b}{2}\sin(\frac{\theta_0}{l}x) - y \\ w &= \frac{b}{2}\cos(\frac{\theta_0}{l}x) - y\sin(\frac{\theta_0}{l}x) - \frac{b}{2} \end{aligned} \tag{3.11}$$

where θ_0 is the end twisting rotation; y denotes the coordinate in hoop direction.

The Lagrangian strain tensor can then be calculated

$$\epsilon_{xx} = \frac{\partial u}{\partial x} + \frac{1}{2}[(\frac{\partial u}{\partial x})^2 + (\frac{\partial v}{\partial x})^2 + (\frac{\partial w}{\partial x})^2] = \frac{\theta_0^2 y^2}{2l^2} + \frac{b^2\theta_0^2}{8l^2} \tag{3.12}$$

$$\epsilon_{xy} = \frac{1}{2}[\frac{\partial u}{\partial y} + \frac{\partial v}{\partial x} + (\frac{\partial u}{\partial x}\frac{\partial u}{\partial y} + \frac{\partial v}{\partial x}\frac{\partial v}{\partial y} + \frac{\partial w}{\partial x}\frac{\partial w}{\partial y})] = \frac{b\theta_0}{4l} \tag{3.13}$$

and the strain rates

$$\dot{\epsilon}_{xx} = [(\frac{y}{l})^2 + \frac{1}{4}(\frac{b}{l})^2]\theta_0 \cdot \dot{\theta}_0 \tag{3.14}$$

$$\dot{\epsilon}_{xy} = \frac{1}{4}(\frac{b}{l}) \cdot \dot{\theta}_0 \tag{3.15}$$

The other components of the strain and strain rate tensor are zero.

If the tube is axially free at the loaded end, there will be an axial displacement U_0, as shown in Fig.3.2.1. The strain and strain rate in X direction will become

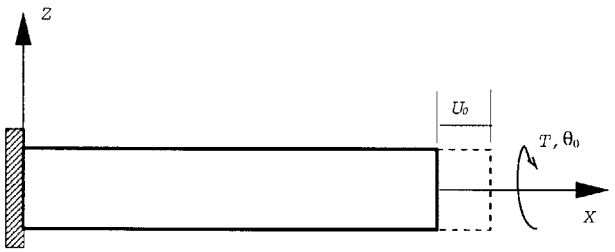

Figure 3.2: An axially free tube with displacement U_0

$$\epsilon_{xx} = \frac{\theta_0^2 y^2}{2l^2} + \frac{b^2\theta_0^2}{8l^2} - \frac{U_0}{l}$$

$$\dot{\epsilon}_{xx} = [(\frac{y}{l})^2 + \frac{1}{4}(\frac{b}{l})^2]\theta_0 \cdot \dot{\theta}_0 - \frac{\dot{U}_0}{l} \tag{3.16}$$

(3.17)

Applying the principle of virtual work and substituting the above expressions of strain rate into Eq.(3.10) finally results in the following expression for the torsional

resistance. The algebraic details can be found in Appendix A and more details in reference [13].

$$\tau = 0.05r^2\theta_0^2 + 0.58 \tag{3.18}$$

where θ_0 is the end twisting rotation angle; r is the width-length ratio of the tube,

$$r = \frac{b}{l} \tag{3.19}$$

and τ is the dimensionless twisting moment defined by

$$\tau = \frac{T}{2\sigma_0 b^2 t} \tag{3.20}$$

where T is the physical twisting moment; σ_0 denotes the plastic flow stress of the material; b and t are width and wall thickness of the tube, respectively. Note that it will make more physical sense to normalize the twisting moment T by $\frac{2}{\sqrt{3}}\sigma_0 b^2 t$, considering that the fully plastic shear stress is $\sigma_0/\sqrt{3}$.

3.2.2 Cross-section Buckling

Sectional buckling will begin when the twisting rotation reaches a certain angle (critical twisting rotation). During buckling, the walls deform inward. This relieves the membrane strains and reduces the load-carrying capacity of the tube. In the present analysis, a sinusoidal sectional buckling mode is assumed (see Fig.3.3) and a sinusoidal-spiral deformation is developed in the tube(see Fig.3.4 and Fig.3.5). The sectional distortion is the largest at the mid-section of the tube and it decreases to zero at the two ends. Meanwhile, the collapsing sections rotate with angles assumed to vary linearly from one end to the other. The amplitude of the sectional deformation at each section is related to the rotation angle via the geometry of the problem and an assumption of inextensibility in the hoop direction of the wall.

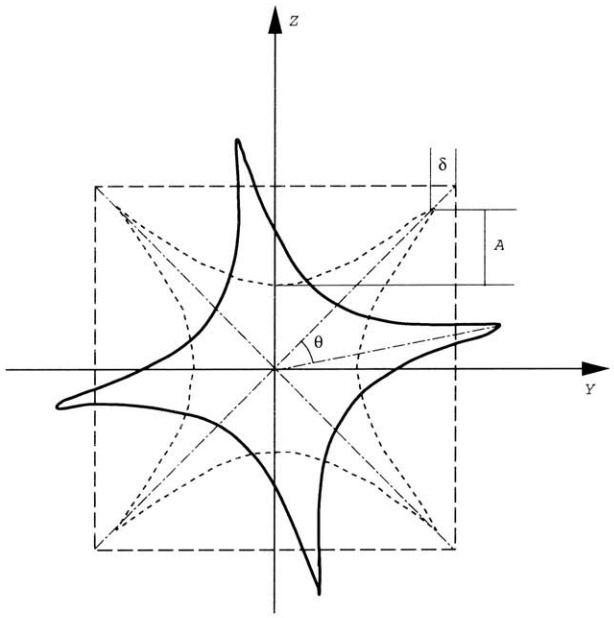

Figure 3.3: Buckling deformation of the cross-section under torsion

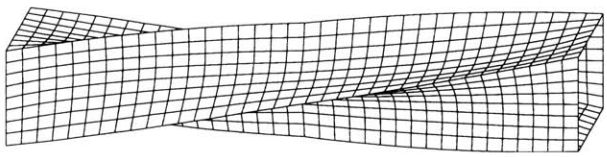

Figure 3.4: Buckling deformation of a square tube under torsion

Consider a buckling section shown in Fig.3.3. The dotted lines denote a virtually deformed section before twisting rotation. The solid lines represent the buckling section with a rotation angle θ. From the geometry, the displacement of the upper flange at this section can be obtained

$$\begin{aligned} v &= (y - \delta \sin \frac{\pi y}{b}) \cos\theta + (\frac{b}{2} - A \cos \frac{\pi y}{b} - \delta) \sin\theta - y \\ w &= (\frac{b}{2} - A \cos \frac{\pi y}{b}) \cos\theta - (y - \delta \sin \frac{\pi y}{b}) \sin\theta - \frac{b}{2} \end{aligned} \tag{3.21}$$

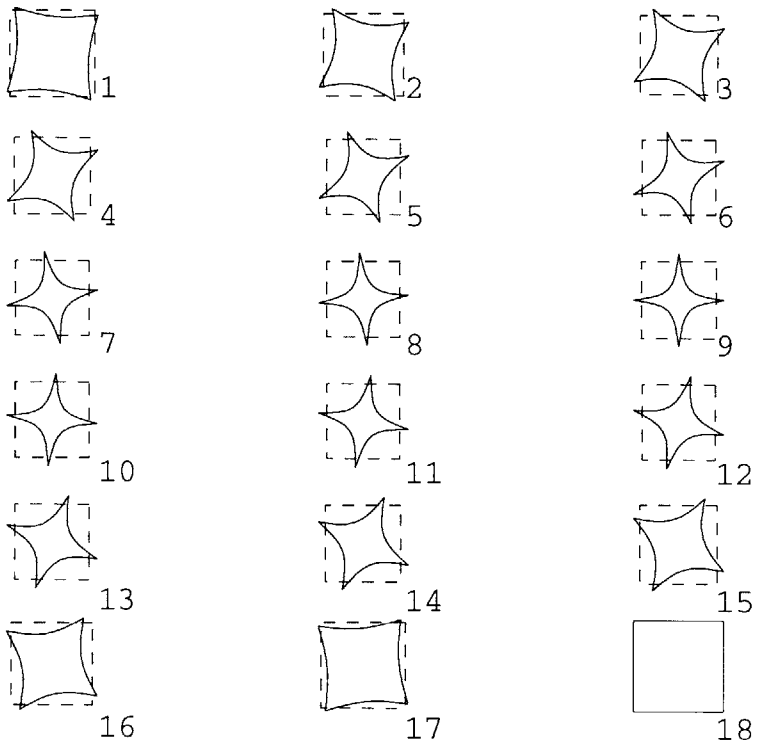

Figure 3.5: Deformed sections along the tube

where θ is the rotation angle at current section, $\theta = \frac{x}{l}\theta_0$; A and δ are two parameters which can be calculated by considering the geometry of the section and the deformation characteristics(see Appendix B for details):

$$\begin{aligned} \delta &= \frac{b}{4}(1-\frac{\sqrt{2}}{2})\frac{4}{\pi}\theta, \qquad (0 \le x \le \frac{l}{2}) \\ \delta &= \frac{b}{4}(1-\frac{\sqrt{2}}{2})\frac{4}{\pi}(\theta_0-\theta), \qquad (\frac{l}{2} \le x \le l) \end{aligned} \tag{3.22}$$

and the amplitude A can be approximated by the expression(details can be found in reference [13]):

$$\frac{A}{b} = 0.24(1-e^{-40\frac{\delta}{b}}) \tag{3.23}$$

The expressions for Lagrangian strain and strain rate tensor can be derived in the same manner as in the pre-buckling phase. They are listed in Appendix C.

By employing Eq.(3.10), the torsional resistance in the buckling phase can be found as a function of the twisting rotation θ_0(algebraic details are included in Appendix D):

$$\tau = 0.58 - 0.21r^{-0.22}\theta_0^{0.34} \tag{3.24}$$

where r is width-length ratio of the tube.

3.2.3 Deformation-spreading

At a certain transverse deflection amplitude and corresponding twisting rotation angle (transitional twisting rotation), internal touching occurs at the mid-section of the tube, which is the most-deformed section in this theoretical model. It is hypothesized that the most-deformed section is formed when the twisting rotation $\theta_0 = \frac{\pi}{2}$, i.e.,the transitional twisting rotation $\theta_m = \frac{\pi}{2}$. Fig.3.6 shows the most-deformed section. From this point on, the most-deformed section will spread towards two ends from the mid-section and a most-deformed area will be formed centering at the mid-section with length 2ξ (see Fig.3.7).

From the point of view of energy, the tube in this phase is equivalent to a tube with twisting rotation θ_m and a most-deformed area 2ξ. With the increase of twisting rotation, additional work is done by spreading the most-deformed area, the effect of which is equivalent to the reduction of the length of the tube and thus the growth of the width-length ratio r. Therefore, the effect of deformation spreading can be considered by introducing an equivalent width-length ratio R

$$R = \frac{L_0}{L_0 - \xi}r = \frac{\theta_0}{\theta_m}r \tag{3.25}$$

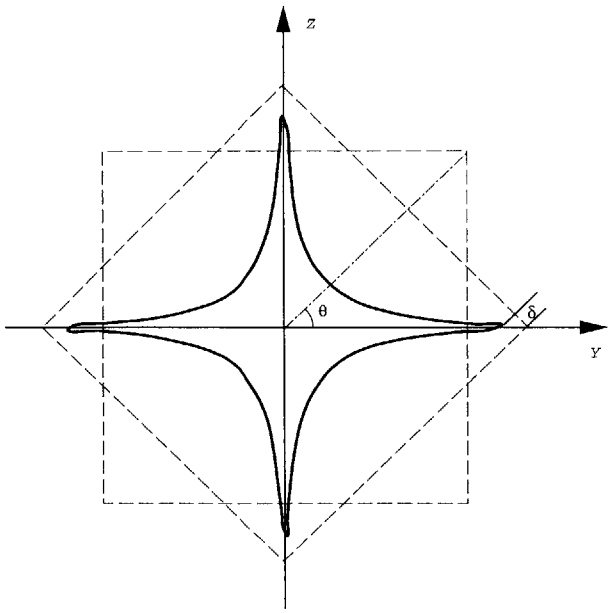

Figure 3.6: Most-deformed section

Hence the torsional resistance in the deformation-spreading phase can be evaluated by replacing the original width-length ratio r in Eq.(3.24) with the above-defined equivalent width-length ratio R

$$\tau = 0.58 - 0.21R^{-0.22}\theta_m^{0.34} = 0.58 - 0.21\frac{\theta_m^{0.56}}{\theta_0^{0.22}}r^{-0.22} \tag{3.26}$$

3.3 Critical Twisting Rotation for Plastic Buckling

The torsional resistance obtained in the previous section shows the weakening geometrical effect on torsional behavior assuming a constant flow stress of the material. The twisting moment τ drops significantly in the buckling phase. However, for a strain-hardening material, the flow stress will be an increasing function of strains.

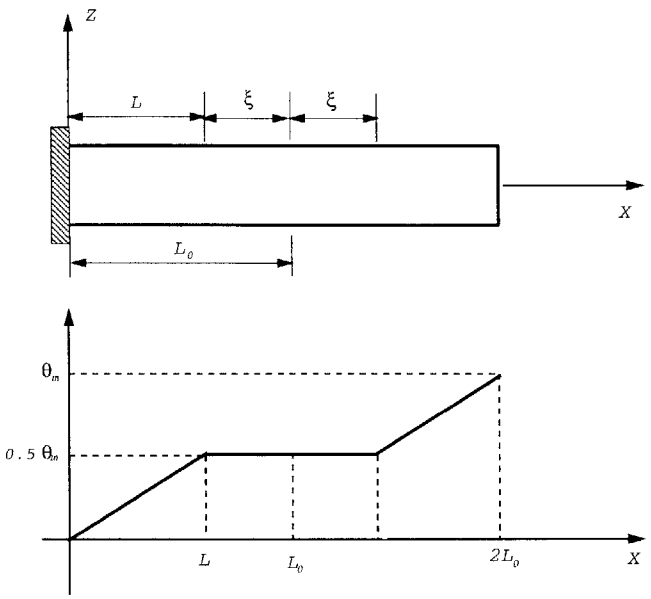

Figure 3.7: Equivalent tube with spreaded most-deformed area when $\theta_0 > \theta_m$

Thus, the torsional resistance of the tube will be determined by the combined effect of geometry and material, and the critical twisting rotation θ_c for sectional plastic buckling will be a minimum on the torque-twist curve.

The stress-strain relationship of the material can be conveniently approximated by the power law

$$\sigma_{eq} = C\epsilon_{eq}^n \tag{3.27}$$

Based on the assumed sinusoidal-spiral buckling mode described in previous section, the average equivalent strain over one flange of the tube can be approximated assuming small θ_0 and $\epsilon_{xx} = 0$

$$\begin{aligned}\epsilon_{eq} &= \frac{1}{bl}\int_S \epsilon_{xy}\, dxdy \\ &= 0.28r\theta_0 - 0.13r\theta_0^2 \\ &= 0.56\bar{\theta_0}(1 - 0.93\frac{\bar{\theta_0}}{r})\end{aligned} \tag{3.28}$$

where $\bar{\theta_0} = \frac{b\theta_0}{2l}$ is the normalized twisting rotation.

By applying Eq.(3.10), a closed-form solution of dimensionless twisting moment τ valid for small θ_0 can be found

$$\tau = 0.65 - 1.18\frac{\bar{\theta_0}}{r} \tag{3.29}$$

The combined effect of geometry and material on the torsional resistance can now be defined as a function $F(\theta_0)$

$$F(\theta_0) = \sigma_{eq} \cdot \tau \tag{3.30}$$

As argued above, the critical twising rotation θ_c for sectional plastic buckling will be such that the function $F(\theta_0)$ reaches a stationary point

$$\frac{dF}{d\theta_0} = 0 \tag{3.31}$$

Solving the above equation for the critical twisting rotation θ_c, one gets

$$\theta_c = \frac{1.1(\sqrt{1+2n} - 1)}{\sqrt{1+2n}} \tag{3.32}$$

where n is the power law exponent of the material; θ_c is in radian.

It is interesting to note that the critical twisting rotation for sectional plastic buckling depends only on the exponent n of the stress-strain law. For a specific material AA6063 T7 (n=0.2), Eq.(3.32) gives $\theta_c = 9.8^o$. This agrees very well with the prediction of the numerical simulations, which gives the critical twisting rotation around 10^o. It should also be pointed out that the validity of Eq.(3.32) is limited to a certain range of length-width ratio. It gives reasonably good prediction for the length-width ratioes considered in the present study ($l/b = 4 \backsim 6.5$). Beyond this range, the equation should be used with caution.

3.4 Comparison Between Approximate Solution and Finite Element Solution

In the previous section, analytical and curve-fitted expression for the torque in three successive phases were obtained:

$$\begin{aligned} \tau &= 0.05r^2\theta_0^2 + 0.58 && (0 \leq \theta_0 \leq \theta_c) \\ \tau &= -0.21r^{-0.22}\theta_0^{0.34} + 0.58 && (\theta_c < \theta_0 \leq \theta_m) \\ \tau &= -0.21R^{-0.22}\theta_m^{0.34} + 0.58 && (\theta_0 > \theta_m) \end{aligned} \tag{3.33}$$

where θ_0 is the twisting rotation(in radian); $\theta_m = \frac{\pi}{2}$; R is defined in Eq.(3.25); r denotes the width-length ratio, $r = b/l$.

The critical twisting rotation for plastic sectional buckling can be evaluated by Eq.(3.32). The physical twisting moment is related to the dimensionless twisting moment by

$$T = 2\sigma_0 b^2 t\tau \tag{3.34}$$

Taking, for instance, that the tube material is AA6063 T7 with plastic flow stress of $\sigma_0 = 105.4N/mm^2$, and taking $b = 50mm$, $\frac{b}{t} = 50$, the twisting moment in pre-buckling, post-buckling and deformation-spreading phase are plotted in Fig. 3.8(solid lines) for tubes with length-width ratio varying from 4 to 6.5. The results of numerical simulations are also shown in the figure for comparison (dashed lines).

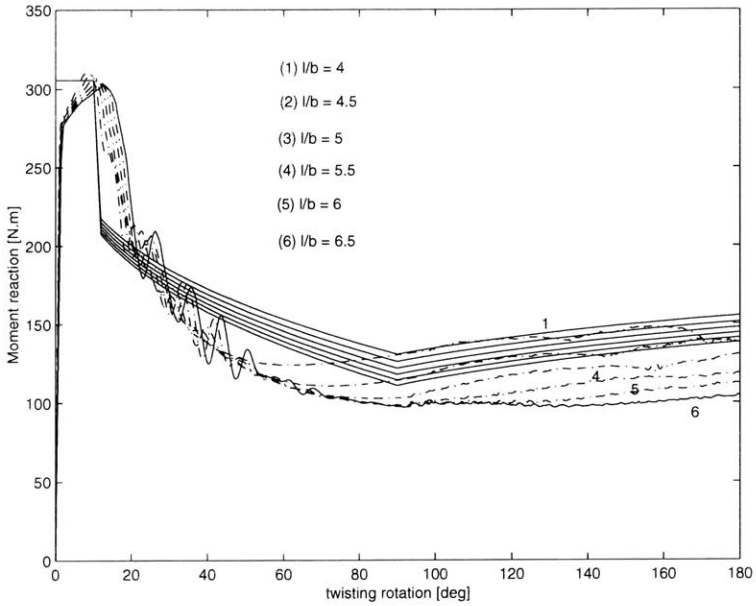

Figure 3.8: Plastic resistance of square tubes of alloy AA6063 T7 (Solid lines:analytical model; dotted lines: FEM results. To normalize, plot $\frac{T}{2\sigma_0 b^2 t}$ vs $\frac{b\theta_0}{l}$ with $\sigma_0 = 105.4MPa$, $t = 1mm$ and corresponding b and l)

As can be seen in the figure, the analytical solutions agree well with the numerical results. The torsional resistance reaches the ultimate value at approximately 10^o at which point the sectional buckling initiates. After that, crushing mechanism take place at sections and the loading resistance drops considerably due to the plastic sectional buckling. At large rotations, the twisting moments appear to assume constant values, which correspond to a stablilized crushing.

Chapter 4

Plastic Resistance of Thin-walled Rectangular and Hexagonal Tubes

The analytical solution obtained in the previous chapter for a square tube will be extended to rectangular and hexagonal tubes. Numerical simulations will be conducted for rectangular and hexaognal tubes and results will be compared with theorectical solutions.

4.1 Approximate Solution

Now consider the torsional crushing of rectangular and hexagonal tubes (shown in Fig.4.1). Due to the similarity in the geometry, we can expect that the torsional behavior of these two tubes will be similar to that of a square tube. Thus, we can assume for simplicity that the dimensionless twisting moments and the critical twisting rotation of rectangular and hexagonal tubes are the same as those of square tube. Therefore, Eq.(3.32) and Eq.(3.33) can be readily applied to the cases of rectangular and hexagonal tubes, with a new width-length ratio r defined as $\frac{b+h}{2l}$ for rectangular tubes.

However, Eq.(3.34) should be revised to calculate physical twisting moment of non-

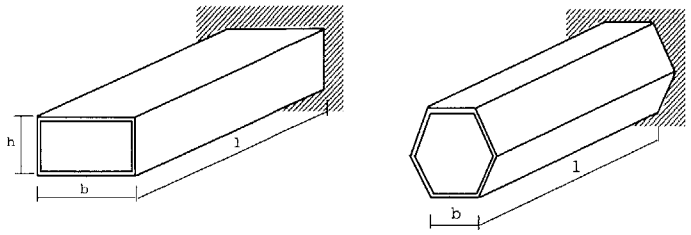

Figure 4.1: Rectangular and hexagonal tubes subjected to torsion

square tubes. One can note that the b^2 term in Eq.(3.34) represents the area enclosed by the cross-section of a square tube [21]. Employing the counterparts of this in rectangular and hexagonal tubes, we can obtain the torsional resistance of a rectangular tube

$$T = 2\tau\sigma_0 bht \tag{4.1}$$

and hexagonal tube

$$T = 3\sqrt{3}\tau\sigma_0 b^2 t \tag{4.2}$$

where τ denotes the dimensionless twisting moment expressed in Eq.(3.33) for pre-buckling, cross-section deforming and deformation-spreading phases.

More generally, the torsional resistance of a prismatic tube can be calculated

$$T = 2\tau\sigma_0 At \tag{4.3}$$

where A is the area enclosed by the cross-section of the tube [21].

The foregoing analytical solutions of rectangular and hexagonal tubes with material AA6063 T7 are plotted in Fig.4.4 and Fig.4.5, respectively. Numerical study was conducted for comparison.

4.2 Numerical Study

Rectangular tubes of $b = 50mm$, $l = 250mm$ and $t = 1mm$ with three different aspect ratios $b/h = 2; 1.5$ and 1.25 were analyzed numerically using the non-linear finite element code $PAM-CRASH^{TM}$. Numerical simulations were also carried out for hexagonal tubes of $l = 250mm$ and $t = 1mm$ with three different width of flanges, $b = 30mm, 40mm$ and $50mm$ respectively. In all cases, a clamped boundary condition is applied at one end of the tube, while the other end is connected to a rigid body mechanism (therefore no warping at the end section). which is allowed to move axially. The twisting rotation is applied quasi-statically at the center of the rigid section. The tube material is aluminum extrusion AA6063 T7, with tensile parameters of Young's modulus $E = 6.9 \times 10^4 N/mm^2$ and initial yield stress $\sigma_y = 86.94 N/mm^2$.

The plastic deformation of rectangular and hexagonal tubes at 90^o twisting rotation are illustrated in Figs.4.2 and 4.3 respectively. It can be seen that, similar to the case of square tubes, inward sectional buckling mode is developed and propagated along the length of the tubes. The moment responses are shown in Fig.4.4 and Fig.4.5, together with the analytical solutions derived above.

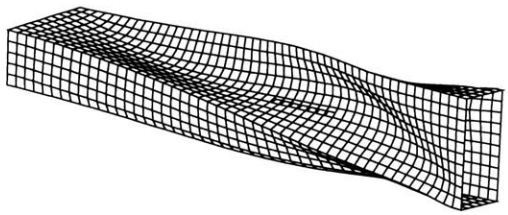

Figure 4.2: Plastic deformation of a rectangular tube at 90^o rotation

As can be seen from the figures, the torsional behavior of thin-walled rectangular and hexagonal tubes can also be characterized by three distinct phases, as in the case of square square tubes, namely pre-buckling, buckling and deformation-spreading phases. In the pre-buckling phase, the tubes show high load resistance which drops

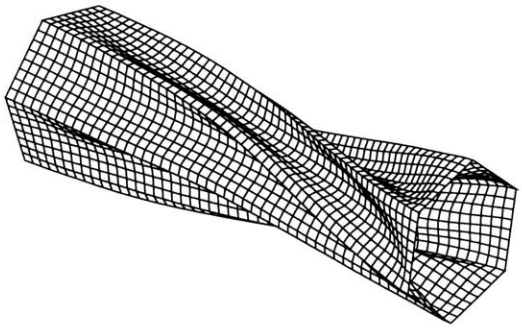

Figure 4.3: Plastic deformation of a hexagonal tube at 90^o rotation

significantly when tubes buckle and appears to assume a nearly constant value in the deformation-spreading phase.

The analytical solution for rectangular tubes compares very well with the numerical results, as can be seen from Fig.4.4, while for hexagonal tubes, it predicts smaller pre-buckling response and critical twisting rotation than numerical results give. It is due to the fact that the analytical solution is based on the geometry of a sqaure tube. The rectangular tube deforms in a similar way as the square tube and the deformation mode of a hexagonal tube is differed.

It should also be noted that, because a hexagonal section has larger corner angles(120^o) than a square section(90^o), it can deform inward more than a square section can. Consequently, the deformation-spreading will be delayed in the hexagonal tube and the transition angle θ_m (which defines a kink in the stabilized phase of response) will be larger than $\pi/2$. This can be observed in the numerical results shown in Fig.3.7 but this property has not been taken into account in the present analytical solution.

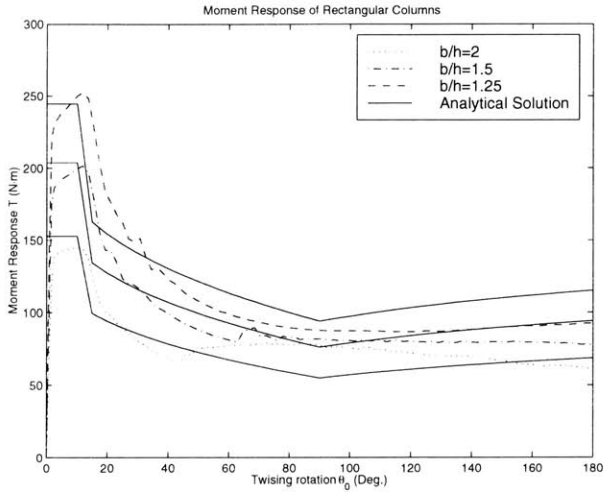

Figure 4.4: Torsional resistance of rectangular tubes($l/b = 5, b/t = 50$)

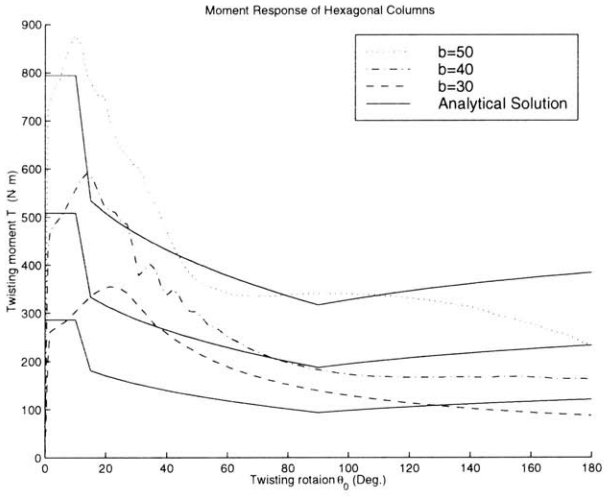

Figure 4.5: Torsional resistance of hexagonal tubes($l = 250mm, t = 1mm$; The unit for b in figure is also mm)

Chapter 5

Experimental Study

Torsional experiments on thin-walled square tubes have been performed to validate the analytical and numerical solutions discussed earlier in this paper. The specimens used in the test were provided by Norsk Hydro ASA, Norway. As a part of the whole project, some foam-filled specimens were also tested and results are reported in this chapter together with those of empty ones, even though the problem of foam-filled thin-walled members is beyond the range of this paper.

5.1 Experimental Setup

Pilot tests were conducted with a torsional actuator with maximum capacity of $2kNm$. But calculations of peak twisting moments showed that such a torsional actuator was not sufficient for the current testing program. In addition, there was not enough axial displacement available on the torsional actuator which is necessary to compensate the shortening of specimen during twisting. Therefore, a completely new testing rig was designed and manufactured, which uses a linear actuator.

Figs.5.1 and 5.2 show the testing apparatus. A simple lever arm design is applied allowing an axial DOF of the loading end of the specimen using a ball bearing. On the other end of the specimen, a clamped fixture represents the loading boundary

condition. The linear actuator is connected with the top of a cardan joint and thereby has all necessary DOFs for the kinematics. The lever arm itself is hinged with the actuator. Care was taken to release any axial force that might have developed during the process of large rotation.

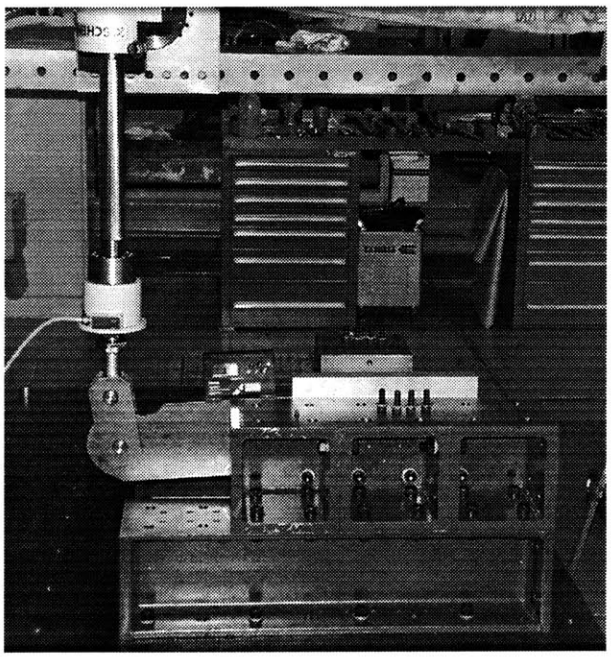

Figure 5.1: Testing rig design

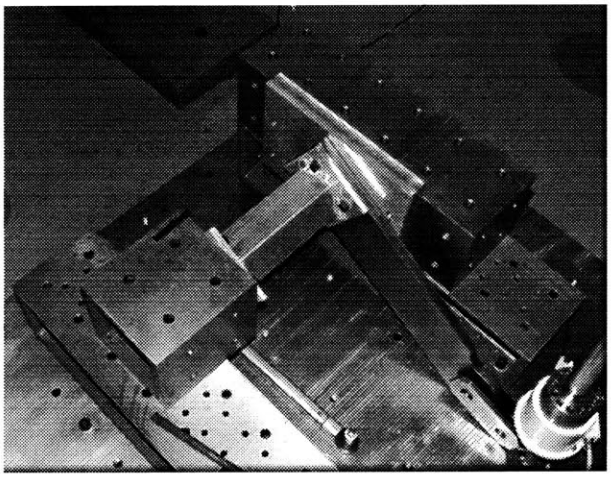

Figure 5.2: Design details of the lever arm

The force and displacement associated with the linear actuator are recorded by force

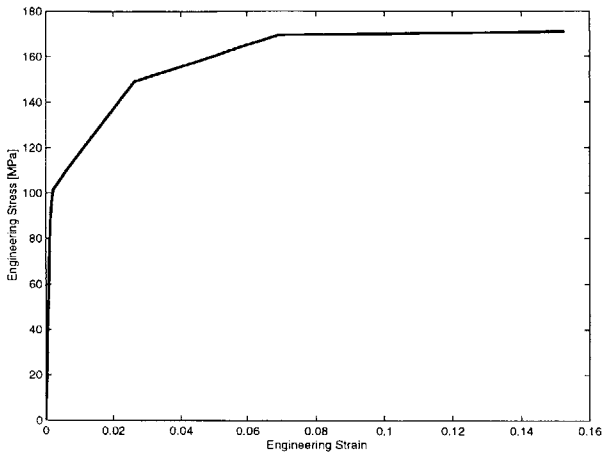

Figure 5.3: Engineering stress-strain curve of AA6063 T7

sensor and displacement sensor, respectively. From the kinematics of the system, these data can be easily converted to twisting moment acting on the specimen and the corresponding twisting angle. The testing rig is integrated into a stiff frame. The fixture of the specimen is mounted on a stiff plate horizontally. The linear actuator is displacement-controlled and powered by a hydraulic supply. The maximum stroke of the actuator is 600mm and its maximum loading capacity is $40kN$. Fig.5.2 shows the details of the lever arm. The range of the twisting angle of the lever arm is $-30^o \sim +30^o$.

The tests were run quasi-statically with an actuator velocity at about $0.8mm/s$. The data sampling frequency is $1Hz$.

5.2 Specimens

The aluminum extrusions and aluminum foams were provided by Norsk Hydro ASA, Norway. The extrusions are square sections with dimension $80mm \times 80mm$, thickness $3mm$ and length $270mm$. The material is AA6063 T7. An engineering stress-strain curve of this material is shown in Fig.5.3.

The aluminum foam has geometry $270 \times 77 \times 77mm$ and were filled into the extrusion

Table 5.1: Specimen Summary

Specimen No.	Type	Foam Weight $[g]$	Foam Density $[g/cm^3]$	Foam Crushing Strength $[MPa]$
S1	empty	0	0	0
S2	empty	0	0	0
S3	filled	220	0.14	1.78
S4	filled	240	0.15	1.97
S5	filled	300	0.19	2.81
S6	filled	300	0.19	2.81
S7	filled	380	0.24	3.99
S8	filled	380	0.24	3.99

sections. Four different foam densities were tesed. Table5.2 summarizes the specimen information.

5.3 Testing Results

The tests were run quasi-statistically. One end of the tube was clamped while the other end was axially free and was subjected to twisting rotation up to 32^o. Some interesting observations were made from the experiment:

(i) The twisting deformation and sectional deformation pattern of empty tube agree generally with the numerical predictions and the analytical model(see Fig.5.4 and Fig.5.5);

(ii) The torsional resistance responses of an empty tube obtained in the test is shown Fig.5.6. The resistances predicted by numerical simulation and analytical solution are shown in the same figure for comparision. It can be noted that the numerical result and analytical solution have reasonably good agreement while the experimental result gives much smaller twisting resistance after the peak moment. This is due to

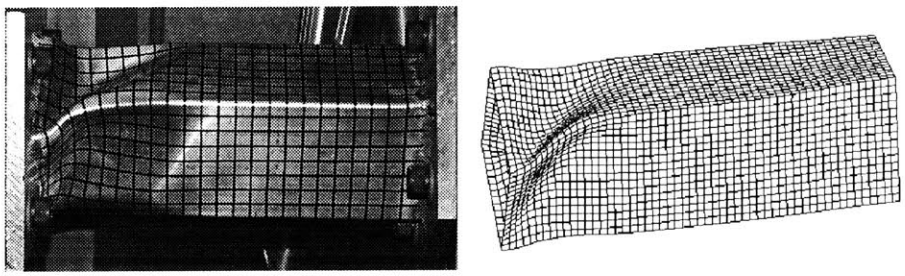

Figure 5.4: Torsional deformation shapes: experimental and numerical

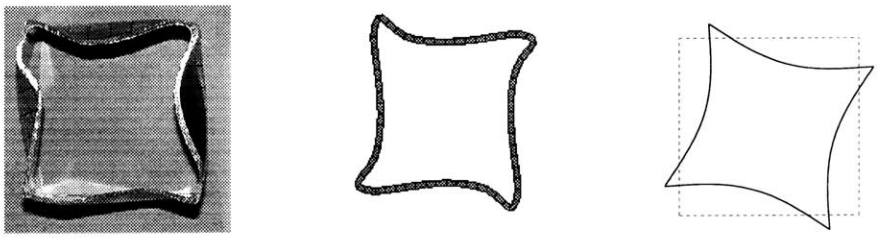

Figure 5.5: Sectional deformation: experimental, numerical and model

an improper design of the end fixture plate of the specimen, which resulted in an unexpected welding failure under large torque, as shown in Fig.5.11. The welding crack, developed in all but one specimen, diminishes significantly the twisting resistance of the specimen after the peak moment.

(iii) The sectional transverse deflection was retarded by the foam-filler, which resulted in a smaller deflection amplitude. The sectional deformations of foam-filled tubes are more localized than that of empty tube. Fig.5.7 and Fig.5.8 show the deformation shape and sectional deformation pattern of one foam-filled tube observed in experiment and predicted numerically. It is evident that the numerical simulation gave fairly good prediction on the deformation;

(iv) Numerical simulations were carried out on two foam-filled tubes with foam filler of density $0.14g/cm^3$ and $0.24g/cm^3$, respectively. The moment responses are shown in Fig.5.9 together with testing results for comparison. As can be seen, two sets of results agree fairly well up to the angle of the peak moment. After that, numerical results predict an increasing resistance while the experiments were stoped because of the fixture failure.

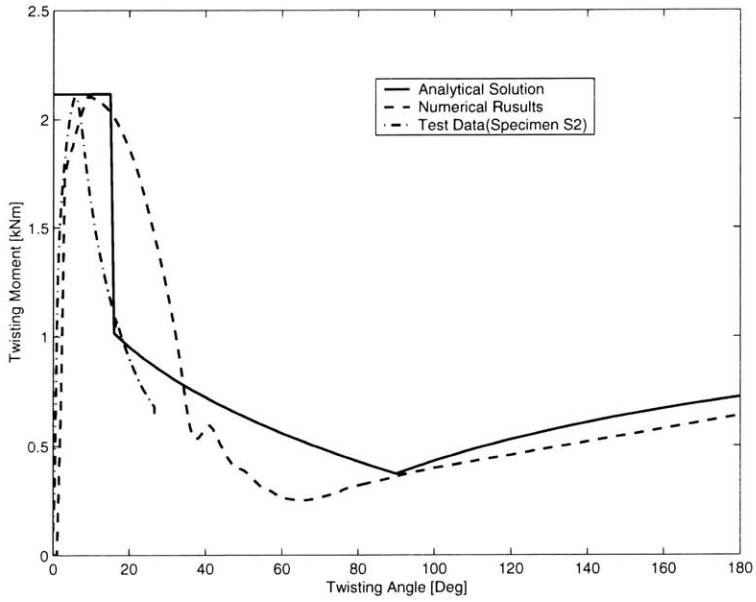

Figure 5.6: Torsional resistance of empty tube:analytical, numerical and experimental (To normalize, plot $\frac{T}{2\sigma_0 b^2 t}$ vs $\frac{b\theta_0}{l}$ withcorresponding b, t, l and σ_0)

(v) Torsional resistance of all tested tubes vs. twisting rotation are plotted in Fig.5.10. Although the tubes lost much of their twisting capacity due to a premature weldment failure during experiment, substantial increase in the energy absorption are still achieved for the foam-filled tubes. This bears an important implication of the attractive potential of the foam-filled thin-walled members as weight-efficient energy-absorbing and force-maintaining structures in collision of a vehicle.

(vi) There are welding failures occuring at the end fixture plate of specimens (Fig.5.11), which resulted in a considerable loss of post-buckling torque of the tubes. A careful re-design of the end fixture for specimens is needed in later experiments of this kind.

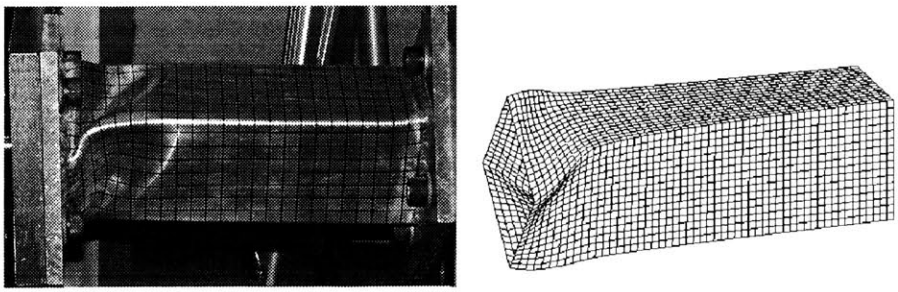

Figure 5.7: Deformation shapes of a foam-filled tube: experimental and numerical

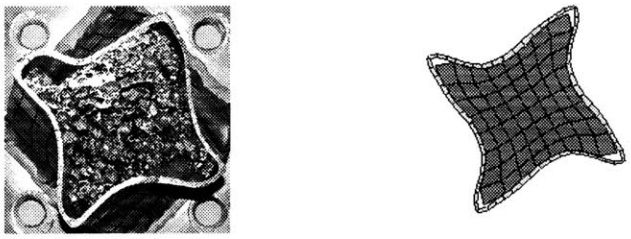

Figure 5.8: Sectional deformation of foam-filled tubes: experimental and numerical

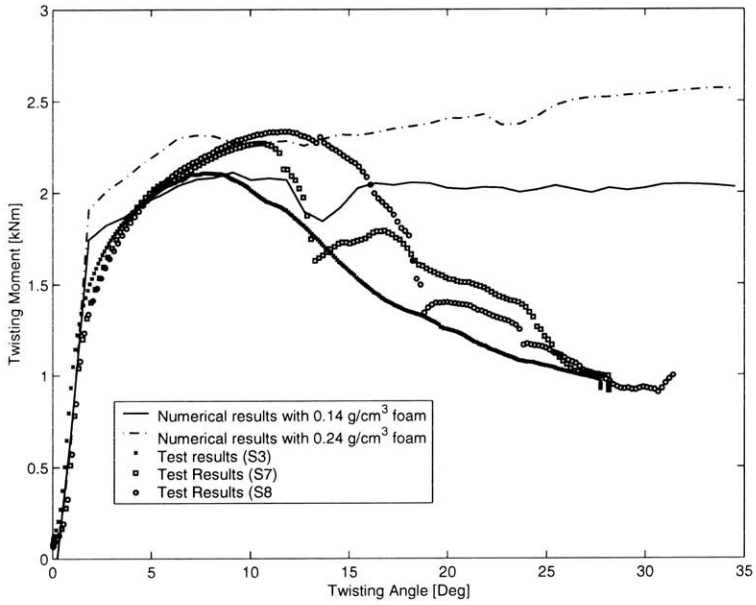

Figure 5.9: Torsional resistance of foam-filled tube: experimental and numerical

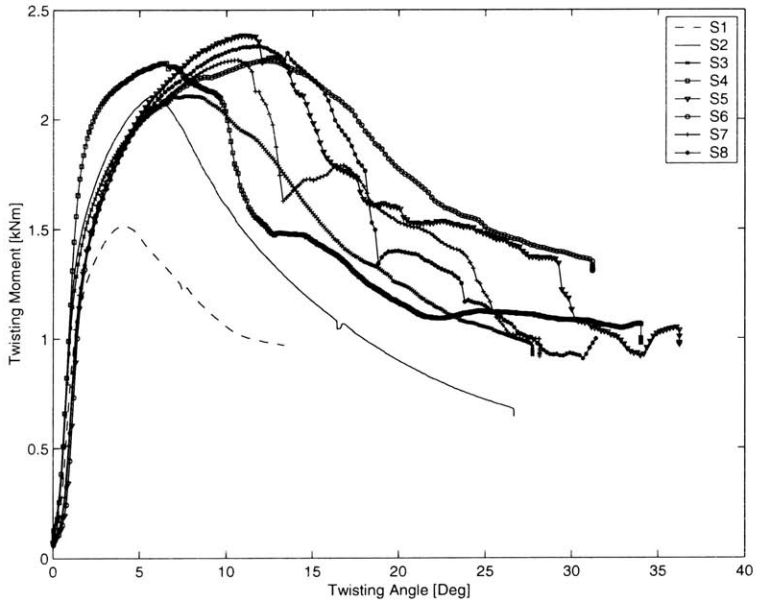

Figure 5.10: Torque-twsit curves for tested specimens(S1 and S2 are empty tubes; the others are foam filled ones)

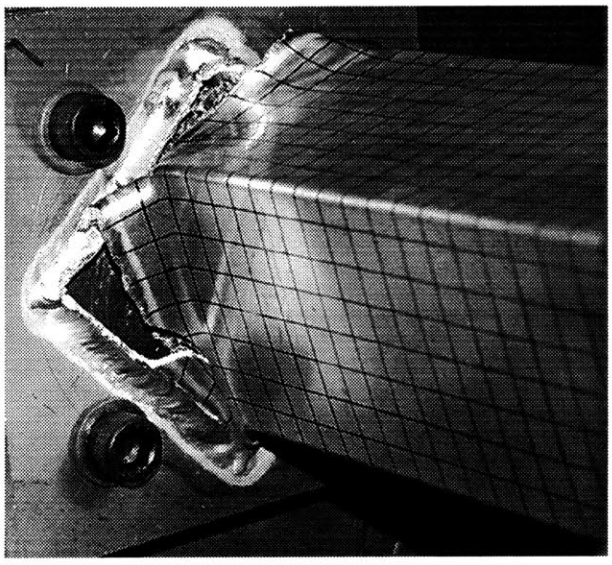

Figure 5.11: Welding failure of the end fixture of a tube

Chapter 6

Discussions

An analysis by applying the principle of virtual work to assumed displacement fields was used to predict the torsional behavior of thin-walled square tubes with large plastic deformations. Three successive deformation phases, namely pre-buckling, cross-section buckling and deformation-spreading phase were identified based on the physical understanding of the torsional behavior of thin-walled prismatic tubes. The analytical model was then extended to the cases of thin-walled rectangular and hexognal tubes. Numerical simulations were carried out and the results are compared with the analytical solutios, giving good agreement.

Torsional experiments on empty and foam-filled square tubes were carried out and results were compared with finite element solutions, and analytical models. A new testing rig was designed, which was able to convert the force on linear actuator to twisting moment on specimen by a specially desgined lever arm. Although the end platens of specimens were not properly designed and unexpected welding failure occured on those fixtures in testing, which diminished significantly the twisting of the tubes, the deformation shape and sectional deformation pattern of empty tubes revealed in the experiment agree well with the numerical predictions and analytical models. The experimental results show increase in plastic resistance and energy absorption for foam-filled tubes compared to empty ones, thus offering potential for thin-walled members with ultralight metal filler as weight-efficent energy-absorbing structures.

In the simple analytical model, the sectional buckling was assumed to initiate at the center of tube and then propagate towards two ends. The most-deformed section was also developed at the center of the tube (see Fig.3.4 and Fig.3.5). In contrast, the finite element solution (see Fig.2.3) and experimental result (see Fig.5.4) exhibit different deformation patterns, in which the initiation of sectional buckling and the most-deformed section are shifted from the center of tube towards one end. Such an assumption on the deformatin mode in the approximate model simplified the analysis while sacrificing to some extent the accuracy of the solution.

More experiments are needed with re-designed end platens to ensure its integrity under large twisting moment. Furthurmore, the present model is restricted to the cases of torsional deformations without warping. In addition to the deformation considered so far, a nonuniform axial displacement may give rise to a warping of the cross-section.

In real applications, torsion seldom acts alone. Usually it is combined with compression and/or bending. The interaction of torsion with compression and bending should be considered in the continuation of the present research.

Of particular interest in crashworthiness application is the effect of the light metal filler, such as aluminum foam and aluminum honeycomb, on the peak and post-buckling torque of a structural member.

Acknowledgement

I wish to thank Professor Tomasz Wierzbicki who as my thesis supervisor has provided me research resources, encouragement and guidance throughout this study. Thanks are also extended to my thesis reader, Professor Frank McClintock, for his inspiring advice.

The present research was conducted for the Core Project of the "Ultralight" Consortium of MIT. The financial support of all members of the Consortium is gratefully acknowledged. Thanks are also due to Altair Computing and Engineering System International for providing free academic licenses of the programs HYPERMESH and PAM-CRASH.

REFERENCES

1 T. Wierzbicki and W. Abramowicz. On the crushing mechanics of thin-walled strucutures. *J. Appl. Mech. 50:pp. 727-739*, 1983.

2 D. Kecman. Bending collapse of rectangular and square section tubes. *Int. J. Mech. Sci., 25(9/10)*, 1983.

3 W. Abramowicz. Simplified crushing analysis of thin-walled columns and beams. *Engng Trans, 29:pp.3-27*, 1983.

4 T. Wierzbicki, W. Abramowicz, T. Gholami, and H. Huang. Stress profiles in thin-walled prismatic columns subjected to crush loading-ii. bending. *Computers & Structures, 51(6):pp. 625-641*, 1994.

5 S. Baba and T. Kajita. Plastic analysis of torsion of a prismatic beam. *International Journal for Numerical Methods in Engineering*, 18(6):927–944, 1982.

6 N.W. Murray. *Introduction to the Theory of Thin-walled Structures.* Clarendon Press, Oxford Engineering Science Series, UK, 1983.

7 M. Mahendran and N.W. Murray. Ultimate load behavior of box-columns under combined loading of axial compression and torsion. *Thin-walled Structures, 9:pp.91-120*, 1990.

8 R.H. White, G.J. Grzebieta and N.W. Murray. Maximum strength of square thin-walled sections subjected to combined loading of torsion and bending. *International Journal of Impact Engineering, 13(2):pp.203-214*, 1993.

9 C. Grant. Network analysis of thin-walled sections in uniform torsion. *Proceedings of the Institute of Mechanical Engineers, Part C, Mechanical Engineering Science, 209(2):pp.133-140*, 1995.

10 S.P. Santosa and T. Wierzbicki. *Effect of an ultralight metal filler on the torsional crushing behavior of thin-walled prismatic columns.* Impact & Crashworthiness Laboratory, Technical Report 5, Masachusetts Institute of Technology, 1997.

11 H. Ma, S. Zhang, and Yang. G. Impact torsional buckling of plastic circular cylinderical shells: Experimental study. *International Journal of Impact Engineering*, 22(1999):531–542, 1999.

12 N.S. Trahair. Plastic torsion analysis of monosymmetric and point-symmetric beams. *Journal of Structural Engineering-ASCE*, 125(2):175–182, 1999.

13 W. Chen and T. Wierzbicki. *Simplified analysis of torsional crushing behavior of thin-walled square columns.* Impact & Crashworthiness Laboratory, Technical Report 8, Masachusetts Institute of Technology, 1998.

14 W. Chen and T. Wierzbicki. Torsional collapse of thin-walled prismatic columns. *Thin-walled Structures*, 36(3):181–196, 2000.

15 W. Chen and T. Wierzbicki. *Torsional Collapse of Foam-filled Thin-walled Columns.* Impact & Crashworthiness Laboratory, Technical Report 19, Massachusetts Institute of Technology, 1998.

16 W. Chen and T. Wierzbicki. Torsional crushing of foam-filled thin-walled square columns. *Submitted to International Journal of Mechanical Science.*

17 T. Belytschko, R.L. Chiapetta, and H.D. Bartel. Efficient large scale non-linear transient analysis by finite elements. *International Journal for Numerical Methods in Engineering*, 10:579–596, 1976.

18 S.P. Santosa. Summary report on crush response of ultralight structures. *Impact and Crashworthiness Laboratory, Technical Report, Massachusetts Institute of Technology*, (24), 1999.

19 T. Wierzbicki and Abramowicz W. The mechanics of deep plastic collapse of thin-walled structures. *In Jones, N. and Wierzbicki, T. editors, Structural Failures, John Wiley*, 1989.

20 Abramowicz W. The macro element approach in crash calculations. *In Ambrosio, Pereira and Silva editors, Crashworthiness of Transportation Systems:Structural Impact and Occupant Protection, Kluwer*, 1997.

21 I.H. Shames. *Introduction to Solid Mechanics.* Prentice Hall, New Jersey, 1989.

Appendices

A Plastic Resistance Calculation in the Pre-buckling Phase

Writing $\eta = \frac{\dot{U}_0}{l \cdot \dot{\theta}_0}$, and substituting Eq.(3.15) and Eq.(3.17) into Eq.(3.10) give a dimensionless torque τ

$$\tau = \frac{T}{2\sigma_0 b^2 t} = \frac{4}{\sqrt{3}} \frac{1}{r^2} \int_{-0.5r}^{0.5r} \sqrt{[(p^2 + 0.25r^2)\theta_0 - \eta]^2 + (0.25r)^2}\, dp \tag{A.1}$$

Because the tube can displace freely in X direction, the axial displacement U_0 should be adjusted so as to minimize the plastic work and therefore the torque moment τ. Thus, η can be determined from

$$\frac{d\tau}{d\eta} = 0 \tag{A.2}$$

Which gives

$$\eta = 0.25\theta_0 r^2 \tag{A.3}$$

Therefore, τ has the form

$$\tau = \frac{4}{\sqrt{3}} \frac{1}{r^2} \int_{-0.5r}^{0.5r} \sqrt{p^4\theta_0^2 + (0.25r)^2}\, dp \tag{A.4}$$

Integrating Eq.(A.4) numerically and curve-fitting the data result in the following expression for dimensionless torsional resistance(details of curve-fitting can be found in reference [13]):

$$\tau = 0.05r^2\theta_0^2 + 0.58 \tag{A.5}$$

B Approximation of the Parameters A and δ in the Buckling Model

Fig.3.6 shows the most distorted section at $\theta = \frac{\pi}{4}$. Because of the assumed inextensibility of the geometry, the rotated vertices move inward by the amount δ

$$\delta = \frac{b}{4}(1 - \frac{\sqrt{2}}{2}) \tag{B.1}$$

Assuming δ at any section within $0 \leq x \leq \frac{l}{2}$ is proportional to the twisting angle at that section, and proportional to $(\theta_0 - \theta)$ at section with $\frac{l}{2} \leq x \leq l$, δ can then be estimated:

$$\begin{aligned} \delta &= \frac{b}{4}(1 - \frac{\sqrt{2}}{2})\frac{4}{\pi}\theta, \qquad (0 \leq x \leq \frac{l}{2}) \\ \delta &= \frac{b}{4}(1 - \frac{\sqrt{2}}{2})\frac{4}{\pi}(\theta_0 - \theta), \qquad (\frac{l}{2} \leq x \leq l) \end{aligned} \tag{B.2}$$

On the assumption of the inextensibility in width direction of the tube during the collapse, the length of the cosine curve remains always constant b. The amplitude A of the cosine curve is determined by the condition

$$\int_{-\frac{b}{2}}^{\frac{b}{2}} \sqrt{(1 - \delta\frac{\pi}{b}\cos\frac{\pi y}{b})^2 + (A\frac{\pi}{b}\sin\frac{\pi y}{b})^2}\, dy_0 = b \tag{B.3}$$

Writing $y = p \cdot b$, $\alpha = \frac{\delta}{b}$ and $\beta = \frac{A}{b}$in Eq.(B.3) gives

$$\int_{-0.5}^{0.5} \sqrt{(1 - \alpha\pi \cos p\pi)^2 + (\beta\pi \sin p\pi)^2}\, dp = 1 \tag{B.4}$$

By solving Eq.(B.4) numerically and curve-fitting the data with an exponential function, an approximate relationship between A, δ and b is obtained:

$$\frac{A}{b} = 0.24(1 - e^{-40\frac{\delta}{b}}) \tag{B.5}$$

C Lagrangian Strain and the Rate of Strain Tensors in the Buckling Phase

In the following expressions, $p = \frac{y}{b/2}$ and $q = x/l$.

$\underline{0 \le x_0 \le \frac{l}{2}}$

$$\begin{aligned}
\epsilon^1_{xx} = {} & .07126\,\theta_0^2\,r^2 + .0004\,\theta_0^2\,r^2\cos(q\,\theta_0)^2\cos(1.571\,p)^2\,e^{(-7.460\,q\,\theta_0)} \\
& - .0005\,\theta_0^2\,r^2\cos(q\,\theta_0)^2\cos(1.571\,p)\,\%1 + .008712\,\theta_0^4\,r^2\,q^2 \\
& - .08408\,\theta_0^3\,r^2\,q\sin(1.571\,p)\,\%1\cos(1.571\,p) + .04660\,\theta_0^2\,r^2\,p \\
& - .02238\,\theta_0^2\,r^2\cos(1.571\,p)\,\%1\sin(1.571\,p) - .04660\,\theta_0^3\,r^2\,q \\
& - .04660\,\theta_0^3\,r^2\,p\,q\sin(1.571\,p) - .02238\,\theta_0^3\,r^2\cos(1.571\,p)\,\%1\,q \\
& + .02444\,\theta_0^2\,r^2\cos(1.571\,p)^2 - .004356\,\theta_0^4\,r^2\,q^2\cos(1.571\,p)^2 \\
& + .4477\,\theta_0^2\,r^2\,p\,\%1\cos(1.571\,p) + .4295\,\theta_0^2\,r^2\cos(1.571\,p)^2\,e^{(-7.460\,q\,\theta_0)} \\
& + .02238\,\theta_0^2\,r^2\cos(1.571\,p)\sin(1.571\,p) + .02238\,\theta_0^3\,r^2\cos(1.571\,p)\,q \\
& - .05760\,\theta_0^2\,r^2\cos(1.571\,p)^2\,\%1 + .1250\,\theta_0^2\,r^2\,p^2 + .2041\,\theta_0^2\,r^2\,\%1\cos(1.571\,p) \\
& - .1200\,\theta_0^2\,r^2\cos(1.571\,p) - .04660\,\theta_0^2\,r^2\sin(1.571\,p) \qquad \text{(C.1)} \\
\%1 := {} & e^{(-3.730\,q\,\theta_0)}
\end{aligned}$$

$$\epsilon^1_{xy} = -.08177\,r\,\theta_0\sin(1.571\,p) + .2500\,r\,\theta_0 - .1200\,r\,\theta_0\cos(1.571\,p)$$

$$
\begin{aligned}
&- .07324\, r\, \theta_0^2 \cos(1.571\, p)\, q - .1885\, r\, \theta_0\, p \sin(1.571\, p) \\
&- .3377\, r\, \theta_0\, \%1 \cos(1.571\, p) \sin(1.571\, p) + .1885\, r\, \theta_0\, p \sin(1.571\, p)\, \%1 \\
&+ .3377\, r\, \theta_0\, e^{(-7.460\, q\, \theta_0)} \cos(1.571\, p) \sin(1.571\, p) - .03514\, r\, \theta_0^2\, q\, \%1 \\
&+ .1200\, r\, \theta_0 \cos(1.571\, p)\, \%1 - .01149\, r\, \theta_0^2\, q + .01369\, r\, \theta_0^3\, q^2 \cos(1.571\, p) \\
&+ .01369\, r\, \theta_0^2 \sin(1.571\, p)\, q \cos(1.571\, p) + .03514\, r\, \theta_0 \sin(1.571\, p)\, \%1 \qquad \text{(C.2)} \\
&\%1 := e^{(-3.730\, q\, \theta_0)}
\end{aligned}
$$

$$
\begin{aligned}
\dot{\epsilon}_{xx}^1 = [&-.2401\, \theta_0\, r^2 \cos(1.571\, p) - .021\, \theta_0^2\, r^2 \cos(q\, \theta_0)^2 \cos(1.571\, p)^2\, e^{(-7.460\, q\, \theta_0)}\, q \\
&+ .8637\, \theta_0\, r^2 \cos(1.571\, p)^2\, e^{(-7.460\, q\, \theta_0)} + .0007\, \theta_0^2\, r^2 \cos(q\, \theta_0)^2\, q\, \%1 \cos(1.571\, p) \\
&+ .0001\, \theta_0\, r^2 \cos(q\, \theta_0)^2\, \%1 \cos(1.571\, p) \\
&- .2000\, 10^{-5}\, \theta_0\, r^2 \cos(q\, \theta_0)^2 \cos(1.571\, p)^2 - 3.161\, \theta_0^2\, r^2\, e^{(-7.460\, q\, \theta_0)} \cos(1.571\, p)^2\, q \\
&+ .8959\, \theta_0\, r^2\, p \cos(1.571\, p)\, \%1 - .1399\, \theta_0^2\, r^2\, p \sin(1.571\, p)\, q \\
&+ .3161\, \theta_0^3\, r^2\, q^2 \sin(1.571\, p)\, \%1 \cos(1.571\, p) + .03484\, \theta_0^3\, r^2\, q^2 \\
&- .01742\, \theta_0^3\, r^2\, q^2 \cos(1.571\, p)^2 - .1671\, \theta_0^2\, r^2\, q \sin(1.571\, p) \cos(1.571\, p)\, \%1 \\
&+ .2147\, \theta_0^2\, r^2\, \%1 \cos(1.571\, p)^2\, q - .04476\, \theta_0\, r^2 \cos(1.571\, p)\, \%1 \sin(1.571\, p) \\
&+ .08321\, \theta_0^3\, r^2\, \%1 \cos(1.571\, p)\, q^2 + .04476\, \theta_0\, r^2 \cos(1.571\, p) \sin(1.571\, p) \\
&+ .4070\, \theta_0\, r^2 \cos(1.571\, p)\, \%1 - .1399\, \theta_0^2\, r^2\, q - .1153\, \theta_0\, r^2 \cos(1.571\, p)^2\, \%1 \\
&- 1.671\, \theta_0^2\, r^2\, p\, q\, \%1 \cos(1.571\, p) + .2501\, \theta_0\, r^2\, p^2 - .8321\, \theta_0^2\, r^2\, q\, \%1 \cos(1.571\, p) \\
&+ .06714\, \theta_0^2\, r^2\, q \cos(1.571\, p) + .09327\, \theta_0\, r^2\, p + .04891\, \theta_0\, r^2 \cos(1.571\, p)^2 \\
&+ .1424\, \theta_0\, r^2 - .09327\, \theta_0\, r^2 \sin(1.571\, p)]\dot{\theta}_0 \qquad \text{(C.3)} \\
\%1 := &\, e^{(-3.730\, q\, \theta_0)}
\end{aligned}
$$

$$
\begin{aligned}
\dot{\epsilon}_{xy}^1 = [&-.00004\, r \cos(q\, \theta_0)^2\, q\, \theta_0 + .1311\, r\, q^2\, \theta_0^2\, \%1 \\
&- 2.521\, r\, \theta_0\, q\, e^{(-7.460\, q\, \theta_0)} \cos(1.571\, p) \sin(1.571\, p) + .1886\, r\, p \sin(1.571\, p)\, \%1 \\
&- .4475\, r\, q\, \theta_0\, \%1 \cos(1.571\, p) + .3374\, r\, e^{(-7.460\, q\, \theta_0)} \cos(1.571\, p) \sin(1.571\, p) \\
&- .1311\, r\, q\, \theta_0\, \%1 \sin(1.571\, p) - .1886\, r\, p \sin(1.571\, p) \\
&- .7028\, r\, q\, \theta_0\, p\, \%1 \sin(1.571\, p) + 1.260\, r\, \theta_0\, q\, \%1 \cos(1.571\, p) \sin(1.571\, p) \\
&+ .04074\, r\, q^2\, \theta_0^2 \cos(1.571\, p) + .03514\, r \sin(1.571\, p)\, \%1 - .07028\, r\, \theta_0\, q\, \%1 \\
&- .02298\, r\, \theta_0\, q + .02737\, r \sin(1.571\, p)\, \theta_0\, q \cos(1.571\, p) \\
&- .3374\, r\, \%1 \cos(1.571\, p) \sin(1.571\, p) + .2501\, r - .1465\, r\, \theta_0\, q \cos(1.571\, p)
\end{aligned}
$$

$$- .08174\, r \sin(1.571\, p) - .1200\, r \cos(1.571\, p) + .1200\, r\, \%1 \cos(1.571\, p)]\dot{\theta}_0$$
$$\%1 := e^{(-3.730\, q\, \theta_0)} \tag{C.4}$$

$\underline{\frac{l}{2} \leq x_0 \leq l}$

$$\begin{aligned}
\epsilon_{xx}^2 = {} & .4295\, \theta_0^2\, r^2\, e^{(-7.460\, \theta_0)}\, e^{(7.460\, q\, \theta_0)} \cos(1.571\, p)^2 - .04660\, \theta 0^3\, r^2\, p \sin(1.571\, p) \\
& + .008712\, \theta_0^4\, r^2\, q \cos(1.571\, p)^2 - .01742\, \theta_0^4\, r^2\, q \\
& - .08408\, \theta_0^3\, r^2 \sin(1.571\, p)\, q\, e^{(-3.730\, \theta_0)}\, \%1 \cos(1.571\, p) \\
& - .4477\, \theta_0^2\, r^2\, p\, e^{(-3.730\, \theta_0)}\, \%1 \cos(1.571\, p) - .04660\, \theta_0^3\, r^2 \\
& + .02238\, \theta_0^2\, r^2 \sin(1.571\, p) \cos(1.571\, p)\, e^{(-3.730\, \theta_0)}\, \%1 + .07126\, \theta_0^2\, r^2 \\
& + .2036\, \theta_0^2\, r^2\, e^{(-3.730\, \theta_0)}\, \%1 \cos(1.571\, p) - .02238\, \theta_0^3\, r^2\, e^{(-3.730\, \theta_0)}\, \%1 \cos(1.571\, p) \\
& + .02238\, \theta_0^3\, r^2\, e^{(-3.730\, \theta 0)}\, \%1 \cos(1.571\, p)\, q \\
& + .08408\, \theta_0^3\, r^2 \sin(1.571\, p)\, e^{(-3.730\, \theta_0)}\, \%1 \cos(1.571\, p) \\
& - .05760\, \theta_0^2\, r^2 \cos(1.571\, p)^2\, e^{(-3.730\, \theta_0)}\, \%1 - .004356\, \theta_0^4\, r^2 \cos(1.571\, p)^2 \\
& + .008712\, \theta_0^4\, r^2 + .008712\, \theta_0^4\, r^2\, q^2 - .04660\, \theta_0^2\, r^2\, p + .04660\, \theta_0^3\, r^2\, q \\
& + .04660\, \theta_0^3\, r^2\, p\, q \sin(1.571\, p) + .02444\, \theta_0^2\, r^2 \cos(1.571\, p)^2 \\
& - .004356\, \theta_0^4\, r^2\, q^2 \cos(1.571\, p)^2 + .4000\, 10^{-5}\, \theta_0^4\, r^2 \cos(q\, \theta_0)^2\, q \\
& - .02238\, \theta_0^2\, r^2 \cos(1.571\, p) \sin(1.571\, p) \\
& - .02238\, \theta_0^3\, r^2 \cos(1.571\, p)\, q + .02238\, \theta_0^3\, r^2 \cos(1.571\, p) + .1250\, \theta_0^2\, r^2\, p^2 \\
& - .1200\, \theta_0^2\, r^2 \cos(1.571\, p) + .0466\, \theta_0^2\, r^2 \sin(1.571\, p)
\end{aligned} \tag{C.5}$$
$$\%1 := e^{(3.730\, q\, \theta_0)}$$

$$\begin{aligned}
\epsilon_{xy}^2 = {} & .08177\, r\, \theta_0 \sin(1.571\, p) + .2500\, r\, \theta_0 - .1200\, r\, \theta_0 \cos(1.571\, p) \\
& + .07324\, r\, \theta_0^2 \cos(1.571\, p)\, q + .1885\, r\, \theta_0\, p \sin(1.571\, p)\, e^{(-3.730\, \theta 0)}\, \%1 \\
& - .03514\, r\, \theta_0^2\, e^{(-3.730\, \theta_0)}\, \%1 - .02737\, r\, \theta_0^3 \cos(1.571\, p)\, q \\
& - .3377\, r\, \theta_0\, e^{(-7.460\, \theta_0)}\, e^{(7.460\, q\, \theta_0)} \cos(1.571\, p) \sin(1.571\, p) \\
& + .03514\, r\, \theta_0^2\, q\, e^{(-3.730\, \theta_0)}\, \%1 - .01369\, r\, \theta_0^2 \sin(1.571\, p) \cos(1.571\, p) \\
& + .3377\, r\, \theta_0\, e^{(-3.730\, \theta_0)}\, \%1 \cos(1.571\, p) \sin(1.571\, p) \\
& + .1200\, r\, \theta_0 \cos(1.571\, p)\, e^{(-3.730\, \theta_0)}\, \%1 - .1885\, r\, \theta_0\, p \sin(1.571\, p) \\
& - .03514\, r\, \theta_0 \sin(1.571\, p)\, e^{(-3.730\, \theta_0)}\, \%1 - .07324\, r\, \theta_0^2 \cos(1.571\, p)
\end{aligned}$$

$$
\begin{aligned}
&+ .01369\, r\, \theta_0^3 \cos(1.571\, p) + .01149\, r\, \theta_0^2\, q - .01149\, r\, \theta_0^2 \\
&+ .01369\, r\, \theta_0^3\, q^2 \cos(1.571\, p) + .01369\, r\, \theta_0^2 \sin(1.571\, p)\, q \cos(1.571\, p) \qquad \text{(C.6)} \\
&\%1 := e^{(3.730\, q\, \theta_0)}
\end{aligned}
$$

$$
\begin{aligned}
\dot{\epsilon}_{xx}^2 = [&.003900\, \theta_0^2\, r^2 \cos(q\, \theta_0)^2\, e^{(-3.730\, \theta_0)}\, \%2 \cos(1.571\, p)\, q \\
&- 3.182\, \theta_0^2\, r^2\, e^{(-7.460\, \theta_0)}\, \%1 \cos(1.571\, p)^2 + .8643\, \theta_0\, r^2 \cos(1.571\, p)^2\, e^{(-7.460\, \theta_0)}\, \%1 \\
&- .2401\, \theta_0\, r^2 \cos(1.571\, p) + .04476\, \theta_0\, r^2 \cos(1.571\, p)\, e^{(-3.730\, \theta_0)}\, \%2 \sin(1.571\, p) \\
&- .1153\, \theta_0\, r^2 \cos(1.571\, p)^2\, e^{(-3.730\, \theta_0)}\, \%2 + .4070\, \theta_0\, r^2\, e^{(-3.730\, \theta_0)}\, \%2 \cos(1.571\, p) \\
&+ .6321\, \theta_0^3\, r^2 \sin(1.571\, p)\, q\, e^{(-3.730\, \theta_0)}\, \%2 \cos(1.571\, p) \\
&+ 1.671\, \theta_0^2\, r^2\, p\, e^{(-3.730\, \theta_0)}\, \%2 \cos(1.571\, p) + .03484\, \theta_0^3\, r^2 \\
&+ .1671\, \theta_0^2\, r^2 \sin(1.571\, p) \cos(1.571\, p)\, e^{(-3.730\, \theta_0)}\, \%2 \\
&- 1.671\, \theta_0^2\, r^2\, p\, e^{(-3.730\, \theta_0)}\, \%2 \cos(1.571\, p)\, q \\
&- .1671\, \theta_0^2\, r^2 \sin(1.571\, p)\, q \cos(1.571\, p)\, e^{(-3.730\, \theta_0)}\, \%2 - .1399\, \theta_0^2\, r^2 \\
&- .8314\, \theta_0^2\, r^2\, e^{(-3.730\, \theta_0)}\, \%2 \cos(1.571\, p) - .2147\, \theta_0^2\, r^2\, e^{(-3.730\, \theta_0)}\, \%2 \cos(1.571\, p)^2\, q \\
&+ .08321\, \theta_0^3\, r^2\, e^{(-3.730\, \theta 0)}\, \%2 \cos(1.571\, p) \\
&+ 3.182\, \theta_0^2\, r^2\, e^{(-7.460\, \theta_0)}\, \%1 \cos(1.571\, p)^2\, q \\
&- .3161\, \theta_0^3\, r^2 \sin(1.571\, p)\, q^2\, e^{(-3.730\, \theta_0)}\, \%2 \cos(1.571\, p) \\
&+ .08321\, \theta_0^3\, r^2\, e^{(-3.730\, \theta 0)}\, \%2 \cos(1.571\, p)\, q^2 \\
&- .1671\, \theta_0^3\, r^2\, e^{(-3.730\, \theta_0)}\, \%2 \cos(1.571\, p)\, q \\
&- .3161\, \theta_0^3\, r^2 \sin(1.571\, p)\, e^{(-3.730\, \theta_0)}\, \%2 \cos(1.571\, p) \\
&- .8959\, \theta_0\, r^2\, p \cos(1.571\, p)\, e^{(-3.730\, \theta_0)}\, \%2 + .2147\, \theta_0^2\, r^2 \cos(1.571\, p)^2\, e^{(-3.730\, \theta_0)}\, \%2 \\
&+ .8282\, \theta_0^2\, r^2\, e^{(-3.730\, \theta_0)}\, \%2 \cos(1.571\, p)\, q \\
&- .1399\, \theta_0^2\, r^2\, p \sin(1.571\, p) + .1399\, \theta_0^2\, r^2\, p \sin(1.571\, p)\, q + .03484\, \theta_0^3\, r^2\, q^2 \\
&- .01742\, \theta_0^3\, r^2\, q^2 \cos(1.571\, p)^2 + .03483\, \theta_0^3\, r^2\, q \cos(1.571\, p)^2 - .06966\, \theta_0^3\, r^2\, q \\
&- .04476\, \theta_0\, r^2 \cos(1.571\, p) \sin(1.571\, p) + .1399\, \theta_0^2\, r^2\, q + .2501\, \theta_0\, r^2\, p^2 \\
&- .06714\, \theta_0^2\, r^2\, q \cos(1.571\, p) - .09327\, \theta_0\, r^2\, p + .06714\, \theta_0^2\, r^2 \cos(1.571\, p) \\
&+ .04891\, \theta_0\, r^2 \cos(1.571\, p)^2 + .1424\, \theta_0\, r^2 - .01742\, \theta_0^3\, r^2 \cos(1.571\, p)^2 \\
&+ .09327\, \theta_0\, r^2 \sin(1.571\, p) - .02100\, \theta_0^2\, r^2 \cos(q\, \theta_0)^2\, e^{(-7.460\, \theta_0)}\, \%1 \cos(1.571\, p)^2\, q]\dot{\theta}_0 \\
&\%1 := e^{(7.460\, q\, \theta_0)} \\
&\%2 := e^{(3.730\, q\, \theta_0)} \qquad \text{(C.7)}
\end{aligned}
$$

$$
\begin{aligned}
\dot{\epsilon}_{xy}^2 = [&.00004\,r\cos(q\,\theta_0)^2\,q\,\theta_0 - .02298\,r\,\theta_0 - .1886\,r\,p\sin(1.571\,p) \\
&- .1465\,r\,\theta_0\cos(1.571\,p) + .04074\,r\,\theta_0^2\cos(1.571\,p) - .08212\,r\,\theta_0^2\cos(1.571\,p)\,q \\
&+ .04074\,r\,q^2\,\theta_0^2\cos(1.571\,p) + .02298\,r\,\theta_0\,q \\
&+ .02737\,r\sin(1.571\,p)\,\theta_0\,q\cos(1.571\,p) - .02737\,r\sin(1.571\,p)\,\theta_0\cos(1.571\,p) \\
&+ .2501\,r - .00004\,r\cos(q\,\theta_0)^2\,\theta_0 + .1465\,r\,\theta_0\,q\cos(1.571\,p) \\
&+ .4475\,r\,\theta_0\,e^{(-3.730\,\theta_0)}\,\%1\cos(1.571\,p)\,q + .00004\,r\cos(q\,\theta_0)^2\cos(1.571\,p)^2\,\theta_0\,q \\
&+ .1311\,r\,\theta_0^2\,q^2\,e^{(-3.730\,\theta_0)}\,\%1 + .08174\,r\sin(1.571\,p) + .07028\,r\,\theta_0\,q\,e^{(-3.730\,\theta_0)}\,\%1 \\
&+ .1886\,r\,p\sin(1.571\,p)\,e^{(-3.730\,\theta_0)}\,\%1 - .4475\,r\,\theta_0\,e^{(-3.730\,\theta_0)}\,\%1\cos(1.571\,p) \\
&- .1200\,r\cos(1.571\,p) + .7028\,r\,\theta_0\,p\,e^{(-3.730\,\theta_0)}\,\%1\sin(1.571\,p)\,q \\
&+ .1311\,r\,\theta_0\,e^{(-3.730\,\theta_0)}\,\%1\sin(1.571\,p) - .07028\,r\,\theta_0\,e^{(-3.730\,\theta_0)}\,\%1 \\
&- 1.260\,r\,\theta_0\,e^{(-3.730\,\theta_0)}\,\%1\cos(1.571\,p)\sin(1.571\,p) \\
&+ .3374\,r\,e^{(-3.730\,\theta_0)}\,\%1\cos(1.571\,p)\sin(1.571\,p) - .2629\,r\,\theta_0^2\,e^{(-3.730\,\theta_0)}\,\%1\,q \\
&- .1311\,r\,\theta_0\,e^{(-3.730\,\theta_0)}\,\%1\sin(1.571\,p)\,q - .7028\,r\,\theta_0\,p\,e^{(-3.730\,\theta_0)}\,\%1\sin(1.571\,p) \\
&+ 1.260\,r\,\theta_0\,e^{(-3.730\,\theta_0)}\,\%1\cos(1.571\,p)\,q\sin(1.571\,p) \\
&+ .1200\,r\,e^{(-3.730\,\theta_0)}\,\%1\cos(1.571\,p) - .03514\,r\sin(1.571\,p)\,e^{(-3.730\,\theta_0)}\,\%1 \\
&+ .1311\,r\,\theta_0^2\,e^{(-3.730\,\theta_0)}\,\%1 \\
&+ 2.521\,r\,\theta_0\,e^{(-7.460\,\theta_0)}\,e^{(7.460\,q\,\theta_0)}\cos(1.571\,p)\sin(1.571\,p) \\
&- .3374\,r\,e^{(-7.460\,\theta_0)}\,e^{(7.460\,q\,\theta_0)}\cos(1.571\,p)\sin(1.571\,p) \\
&- 2.521\,r\,\theta_0\,e^{(-7.460\,\theta_0)}\,e^{(7.460\,q\,\theta_0)}\cos(1.571\,p)\,q\sin(1.571\,p)]\dot{\theta}_0 \qquad \text{(C.8)} \\
\%1 := &\; e^{(3.730\,q\,\theta_0)}
\end{aligned}
$$

D Torsional Resistance Calculation in the Buckling Phase

The expression for dimensionless torque moment $\tau = \frac{T}{2\sigma_0 b^2 t}$ can be written

$$\tau = \frac{2}{\sqrt{3}}\frac{1}{r}\Big[\int_0^{0.5}\int_{-1}^{1}\sqrt{(\dot{\epsilon}^1_{xx})^2 + (\dot{\epsilon}^1_{xy})^2}\,dpdq + \int_{0.5}^{1}\int_{-1}^{1}\sqrt{(\dot{\epsilon}^2_{xx})^2 + (\dot{\epsilon}^2_{xy})^2}\,dpdq\Big] \quad \text{(D.1)}$$

where $p = \frac{y}{b/2}$, $q = \frac{x}{l}$.

When axially free condition is considered, similar to the case of pre-buckling, assuming an axial displacement U_0 so that the total axial force at $x = \frac{l}{2}$ is zero. The expression for $\frac{\dot{U}_0}{l}$ is given in Appendix E.

Applying Eq.(D.1) and substituting $\dot{\epsilon}_{xx}$ with $(\dot{\epsilon}_{xx} - \frac{\dot{U}_0}{l})$, dimensionless torque moment under axially free condition can be obtained. Fitting the numerical integration data with a power function results in the following expression for τ:

$$\tau = -0.21 r^{-0.22}\theta_0^{0.34} + 0.58 \quad \text{(D.2)}$$

E Calculation of Extension in the Buckling Phase

$$\begin{aligned}
\frac{\dot{U}_0}{l} = [&.09750\,\theta_0\,r^2 - .07689\,\theta_0^2\,r^2 + .006536\,\theta_0^3\,r^2 \\
&+ .0004\,\theta_0\,r^2\cos(.5\,\theta_0)^2\,e^{(-3.730\,\theta_0)} \\
&- .0002\,\theta_0^2\,r^2\cos(.5\,\theta_0)\,e^{(-3.730\,\theta_0)}\sin(.5000\,\theta_0) \\
&- .0007460\,\theta_0^2\,r^2\cos(.5\,\theta_0)^2\,e^{(-3.730\,\theta_0)} + .2022\,\theta_0\,r^2\,e^{(-1.865\,\theta_0)} \\
&- .2100\,\theta_0^2\,r^2\,e^{(-1.865\,\theta_0)} + .4294\,\theta_0\,r^2\,e^{(-3.730\,\theta_0)} - .8008\,\theta_0^2\,r^2\,e^{(-3.730\,\theta_0)} \\
&- .0006366\,\theta_0\,r^2\cos(.5\,\theta_0)^2\,e^{(-1.865\,\theta_0)} \\
&+ .0003183\,\theta_0^2\,r^2\cos(.5\,\theta_0)\,e^{(-1.865\,\theta_0)}\sin(.5000\,\theta_0) \\
&+ .0005936\,\theta_0^2\,r^2\cos(.5\,\theta_0)^2\,e^{(-1.865\,\theta_0)} + .01329\,\theta_0^3\,r^2\,e^{(-1.865\,\theta_0)}]\dot{\theta}_0
\end{aligned} \quad \text{(E.1)}$$